Chapter 02
Materials and experimental methods

2.1 Introduction

The chapter discusses several heat treatment processes, including under-aging(T4), peak-aging(T6), over-aging(T73), and T7352. Such heat treatment likely affects the microstructure evolution thereby the mechanical properties. The interrupted testing with the help of the tensile test involves the partial deformation of AA7075T7352, corresponding to the tensile true strain of 2%, 6%, and 10% for that the first specimen was deformed up to the fracture. Partially tensile deformed alloys were used for the dislocation characterization following the standard procedures. The thermo-mechanical processing technique involves solution quenching in combination with cold rolling (CR) followed by aging. This combination is used to modify the alloy's properties via controlled deformation and heat treatments. The chapter also emphasizes friction stir processing as the central focus. A rotation tool with a threaded pin is used for friction stir processing of the alloys. The FSP is carried out both in the single pass and the multiple passes. In the multiple passes, a maximum of three passes are given to refine the microstructures further. The effect of aging on friction stir processing of AA7075T7352 is also studied in this chapter. The two specific combinations of FSP, and aging are given as: 1. Solution quenching + FSP + peak-aging (SQ+FSP+PA), and 2. FSP+ peak-aging (FSP+PA).

In the first type of processing category, alloys are subjected to solution treatment at 470 °C, for 1h to obtain the single-phase polycrystalline solid solution with increased vacancy concentration. Thereafter, the alloys are subjected to quenching in room temperature water (at 25 °C) thus producing the single-phase supersaturated solid solution (SSSS (α)) with increased vacancy concentration in comparison to room temperature**.** The SQ alloys are subjected to friction stir processing at 1000rpm, thereafter aging (at 120°C) is given for 24 hrs. In the second category, the friction stir-processed alloys (at 1000rpm) were directly

subjected to aging. The chapter also discusses characterization techniques employed for analyzing the alloys. For instance, optical microscope (OM), X-ray diffraction (XRD), scanning electron microscope (SEM), transmission electron microscope (TEM), Differential thermal analyzer (DTA), and Electron back scattered diffraction (EBSD). The techniques used for TEM and EBSD sample preparation and metallographic sample preparation were also discussed. For instance, twin jet electropolishing and Vibromet electro-polishing systems. The chapter also covers details of various mechanical testing methods, e.g. tensile test, interrupted test, Vicker's microhardness, stress corrosion cracking (SCC), etc. The sample geometry and the testing details are also included. At the end of this chapter software details are also discussed.

2.2 Materials

The material is obtained from Deccan Smith Private Limited India, in the plate form ((t > 30mm), with 210 mm length, and 120 mm width) in the form of AA7075T7352. The chemical composition obtained by the electron probe microanalyzer (EPMA) is given in Table 2.1.

Table 2.1 Chemical compositions of the AR alloy AA7075T7352 (Wt%).

Elements	Zn	Mg	Cu	Fe	Cr	Si	Mn	Zr	Ti	Al
Amounts (wt. %)	5.6	2.5	1.6	0.25	0.23	0.2	0.15	0.125	0.1	Bal.

The as-received alloys are heat-treated, and thermo-mechanically processed, thereafter subjected to friction stir processing (FSP). The details of each processing technique are given below:

2.3 Heat treatments

The materials initially arrived in the T7352 temper, especially in AA7075T7352 form. In this temper, the alloys underwent a heat treatment process involving solutionizing at 470ºC for 1 h. Subsequently, it was rapidly quenched in room-temperature water. This particular sample was then subjected to a 10% cold deformation, followed by two stages of ageing treatment. The first stage involved aging at 120ºC for 24 hours, while the second stage, referred to as over-ageing, took place at 160ºC for 30 hours. To obtain the 7075-aluminum alloy in the under-aged (T4), peak-aged (T6), and over-aged (T73) states, four rectangular specimens (each with a cross-sectional area of 1cm² and a length of 70mm) were extracted from the as-received AA7075T7352 plate using a wire cut EDM system. All these specimens were then subjected to a solution heat treatment (470ºC) for 1 h to get the single-phase field thereafter quenched in room temperature water. After solutionizing at 470ºC for 1h and subsequent quenching in room-temperature water, one of the solution-quenched samples underwent natural aging for three months, resulting in the T4 temper (under-aged state). Another set of solution-quenched samples was aged at 120ºC for 24 hours, referred to as peak-ageing, and denoted as the T6 (peak-ageing state) temper. Furthermore, one of the peak-aged (T6) alloys underwent additional aging at 160ºC for 30 hours, a treatment known as over-aging, and was designated as the T73 temper. For a more detailed understanding of the heat treatment cycles for various tempers (e.g., T4, T6, T73, and T7352), the schematics are given in Fig.2.1a-d.

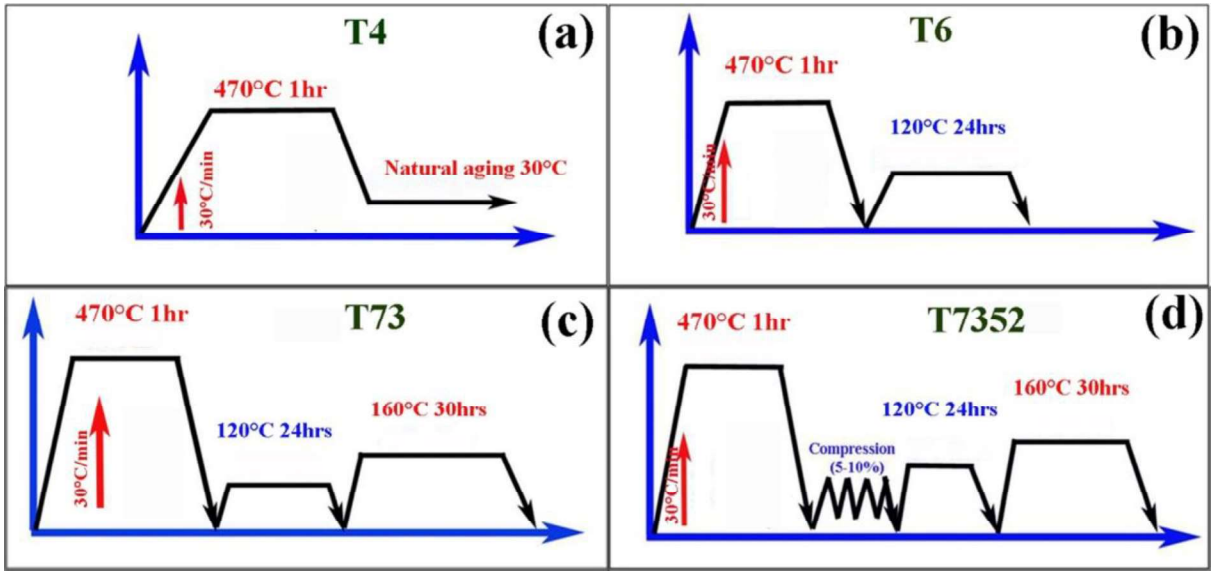

Figs. 2.1a-d. Schematic of heat treatments: (a) under-aging T4, (b) peak-aging T6, (c) over-aging T73, and (d) T7352 temper.

2.4 Interrupted test

The AA7075T7352 alloy was obtained in a rectangular bar shape with dimensions of 105 mm (length) x 10mm (width) x 7mm (thickness). The cutting direction for all four samples was chosen to be parallel to the rolling direction of the as-cast material. This was done to avoid any impact from material orientation and anisotropic effects. Four specimens for tensile testing were prepared according to the ASTM-E8 specification. These specimens are, designated as D1, D2, D3, and D4, and had the dimensions of 30 mm gauge length, 6mm width, and 6mm thickness. The first specimen, D1, was subjected to tensile loading till the fracture. This was done to obtain the maximum percentage elongation (%EL) value and the other mechanical properties like Yield Strength (YS) and Ultimate Tensile Strength (UTS). The tensile data from the fractured specimen was used to obtain the engineering stress vs. engineering strain and true stress vs. true strain plots. The engineering parameters such as the UTS/YS ratio, and the strain hardening exponent (n) are calculated using the curve fitting techniques. The remaining three specimens, namely D2, D3, and D4, were subjected to

partial tensile straining/ deformation. The levels of applied strain are 0.02, 0.06, and 0.1, respectively. These strains are selected below the maximum percentage elongation, which is far away from the point of necking in the material. The deformation was carried out using an Instron 5982 universal testing machine with a capacity of 100 kN. All the tests were conducted at room temperature and a cross-head speed of 1mm/ minute.

2.5 Thermo-mechanical processing

A total of twelve specimens *(dimension: 100mm (l) X 20mm (w) X 6.4mm (t))* are extracted from the as-received AA7075T7352 sheet. All the specimens were subjected to solution treatment at 470 °C for 24 hrs, to get the single-phase solid solution (SSSS(α)) solid solution, thereafter cooled in room temperature water to obtain the single-phase supersaturated solid solution with increased vacancy concentration. All the solution-treated alloys were grouped into six parts, from group 1 to group 6, such that each group contained the two specimens. The first two of them (group 1) were designated as the SQ alloy. Another two solution-treated specimens (group 2) were subjected to peak aging at 120°C, for 24 hrs and they are denoted as T6 alloy.

Next two solution-treated alloys (group 3) were cold deformed to 15% and thereafter subjected to peak-ageing at 120°C, for 24hrs and the specimen is designated as the TMP-1 alloy. The next group of solution-treated alloys (group 4) are cold deformed to 30%, and then subjected to peak aging (120°C, for 24 hrs), which is designated as the TMP-2 alloy. The remaining two specimens (group 5) were cold deformed to 45% and subjected to peak-ageing (T6) treatment, and the processed alloy is symbolically represented as TMP-3. For deciding the amount of cold rolling just after the solution quenching, the first two pieces of alloy plates are cold rolled up to the crack formation, and the maximum percentage reduction was recorded which is found to be ~63% when the crack formation appears. For making the

TMP alloys, three different amounts of cold deformations were given below the maximum percentage reduction, and their details are given in Figs. 2a-e.

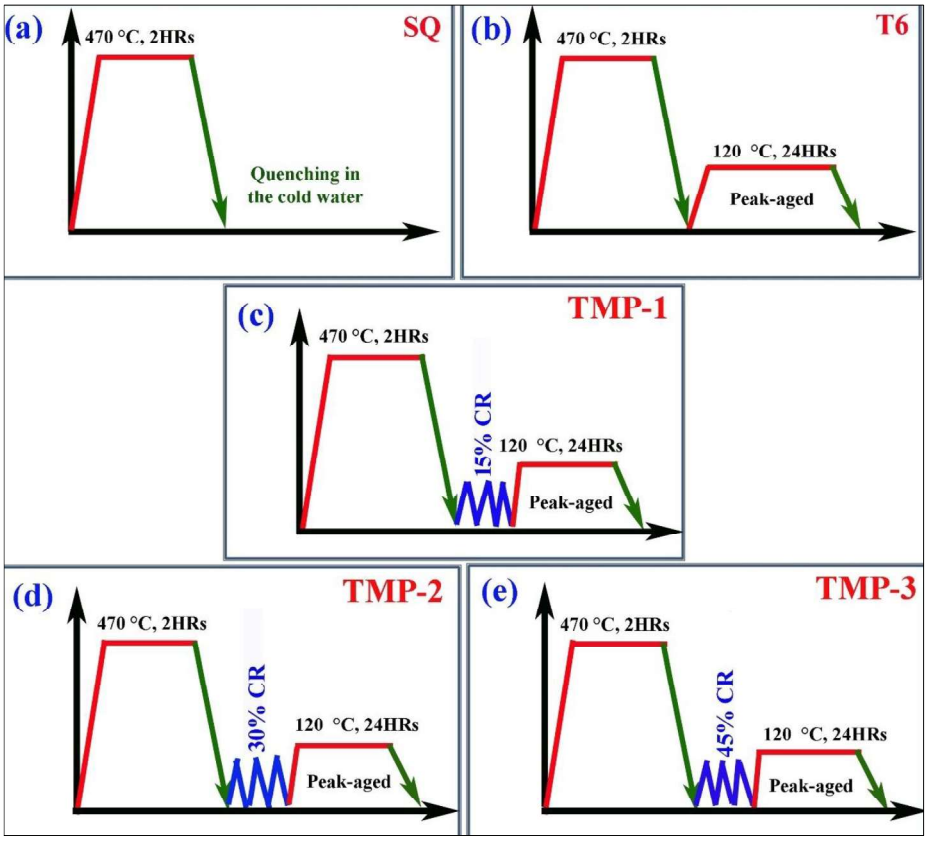

Figs. 2.2a-e. The schematic details of heat treatment and thermo-mechanical processing: (a) SQ, (b) T6, (c) TMP-1, (d) TMP-2, and (e) TMP-3.

2.6 Friction stir processing

Friction Stir Processing (FSP) is a solid-state materials processing technique, which is an extended form of Friction Stir Welding (FSW) originally developed by the Welding Institute in UK in the year 1991. The technique involves the use of the rotating tool, consisting of the shoulder at the wider end and the pin at the lower end. A non-consumable rotating tool with a specially designed pin and shoulder is plunged into the metal sheets to be processed and traversed along the line of interest (Fig. 1). The tool mainly serves two purposes: (a) heating the workpiece, and (b) movement of materials or intermixing to produce the fine and equi-axed grains. Heating is caused by the combined effect of friction between the tool and

workpiece, as well as the plastic deformation. The localized heating softens the alloys at the region close to the tool pin, and combinations of the tool rotation and tool translation lead to the movement of materials from the front of the pin to the back of the pin, producing the solid surface after FSP. Due to the complex geometries of the tools, the movement of materials around the tool pin is quite complex [3]. The alloys experiencing the complex plastic deformation on the account of FSP-assisted elevated temperature give the equiaxed grain in the NZ due to the combined effect of the continuous dynamic re-crystallization (CDRx), and discontinuous dynamic recrystallization (DDRx). Slightly elongated grains in TMAZ arise due to the combined effect of plastic deformation and heating. HAZ produces coarse-grain microstructures due to elevated temperature without plastic deformation. A schematic detail of the working principle of FSP is given in Fig. 2.3.

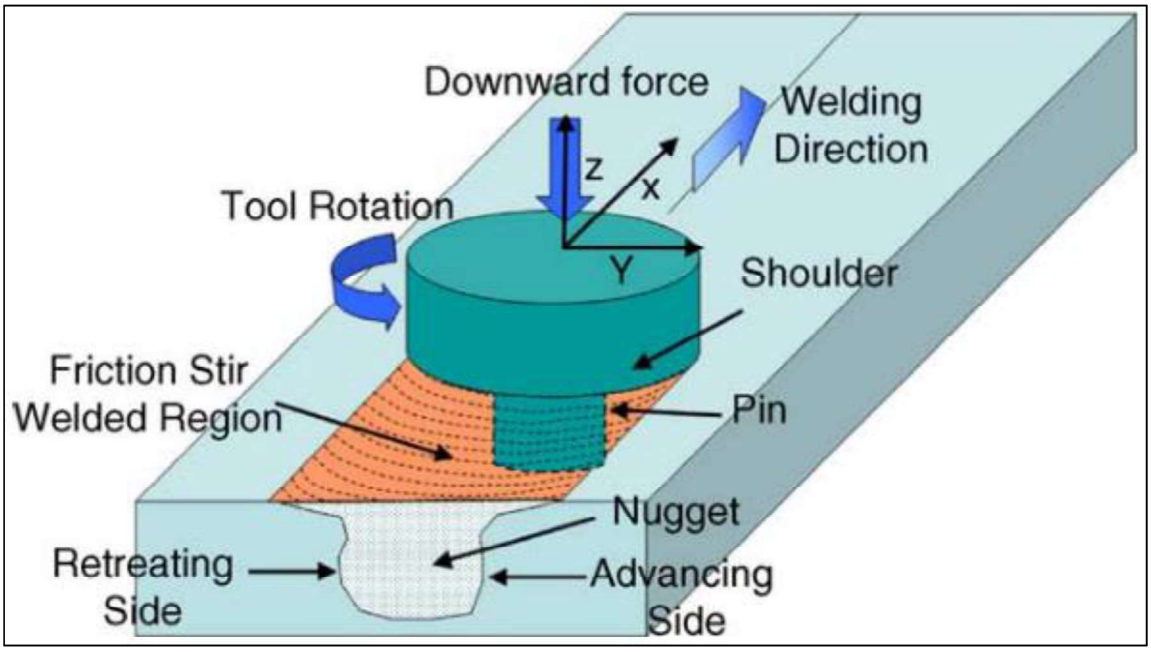

Fig. 2.3 Schematic details of working principles of the FSP [14].

A total of 12 pieces of samples with 200 mm in length, 50 mm in width, and 10 mm in thickness are extracted from the AR alloy sheet. They are subjected to grinding and mechanical polishing. The polished plate is cleaned using the methanol solution to remove

the dirt or scale on its surface, thereafter subjected to the FSP, at the jet thrust of 30 kN. The tool is made using the hardened H-13 tool steel with a 20 mm shoulder diameter, and it was traversed up to a total length of 150 mm at the tool traversed speed of 100mm/min. The pin has the shape of a cone frustum, with a diameter of 8 mm at its wider end and length of a 6 mm. During FSP, a cylindrical tool is plunged into the AA7075T7352 workpiece and traversed along the line of interest upto 150 mm. In multi-pass FSP, materials got overlapped during the processing, and the tool was traversed multiple times on account of requirements of the number of passes. The schematic of FSP setup, and tool used during the alloy processing, along with the stereo images before, and after FSP are given in Figs. 2.4a-e.

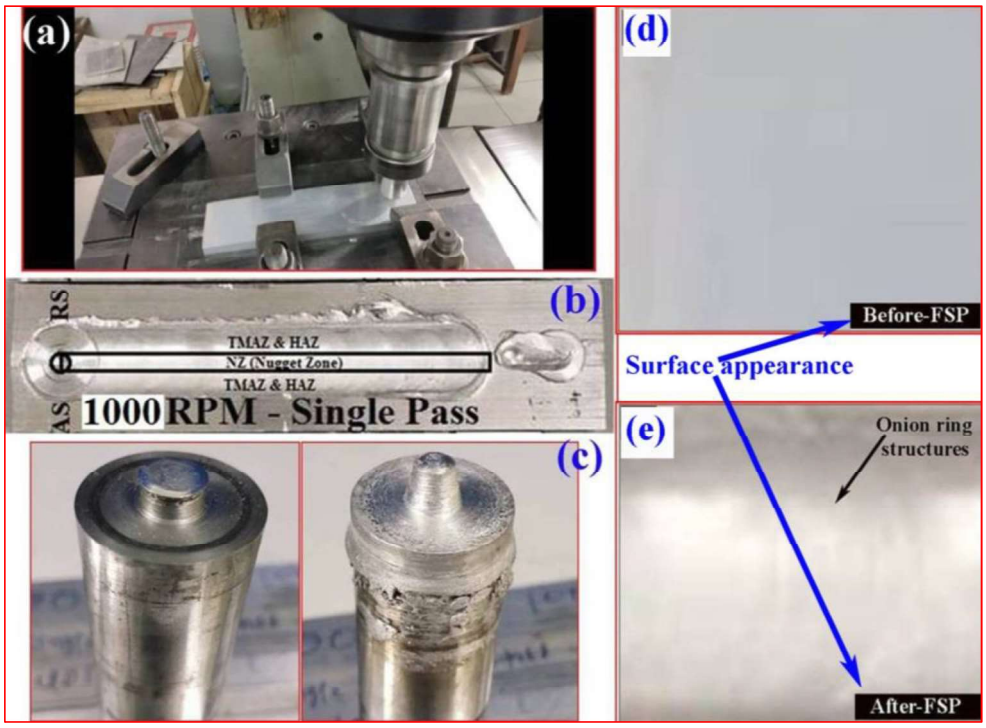

Figs. 2.4 a-e Friction stir processing: experimental set-up and specimen before FSP (a), after FSP (b), A tool used while processing (c), and surface appearance before and after FSP (d,e).

After FSP, one of the processed alloy plates (at 1000 rpm) is subjected to peak-ageing (at 120ºC, for the 24hrs), which is denoted as the FSP+PA alloy. For obtaining the SQ+FSP+PA, combinations of alloy, the base-metal (AA7075T7352) plate is solutionized at 470 ºC, for

1hr, thereafter subjected to FSP at 1000 rpm for 1pass. The processed alloy plate is aged at 120°C, for 24 hrs. The details of processing techniques used to obtain different conditions after FSP are given in Fig. 2.5.

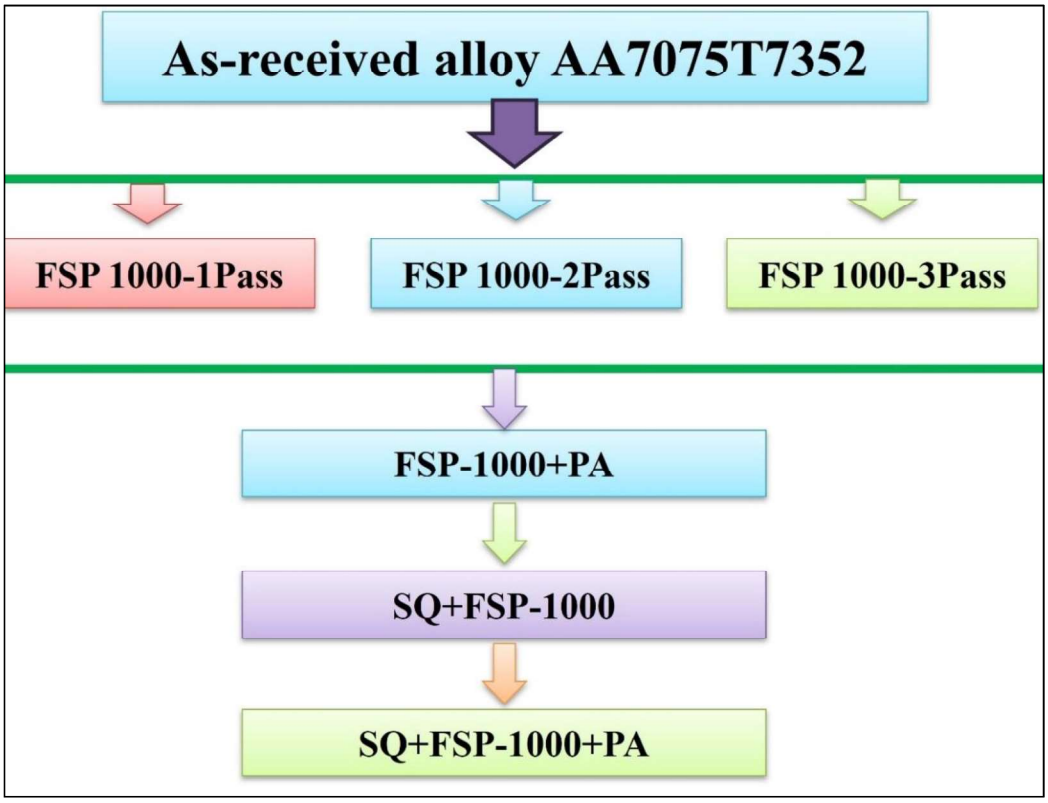

Figs. 2.5 Schematic of the different combinations of the friction stir processing (FSP).

The samples taken from various sections of the processed alloy for various characterization are shown in Fig. 2.6.

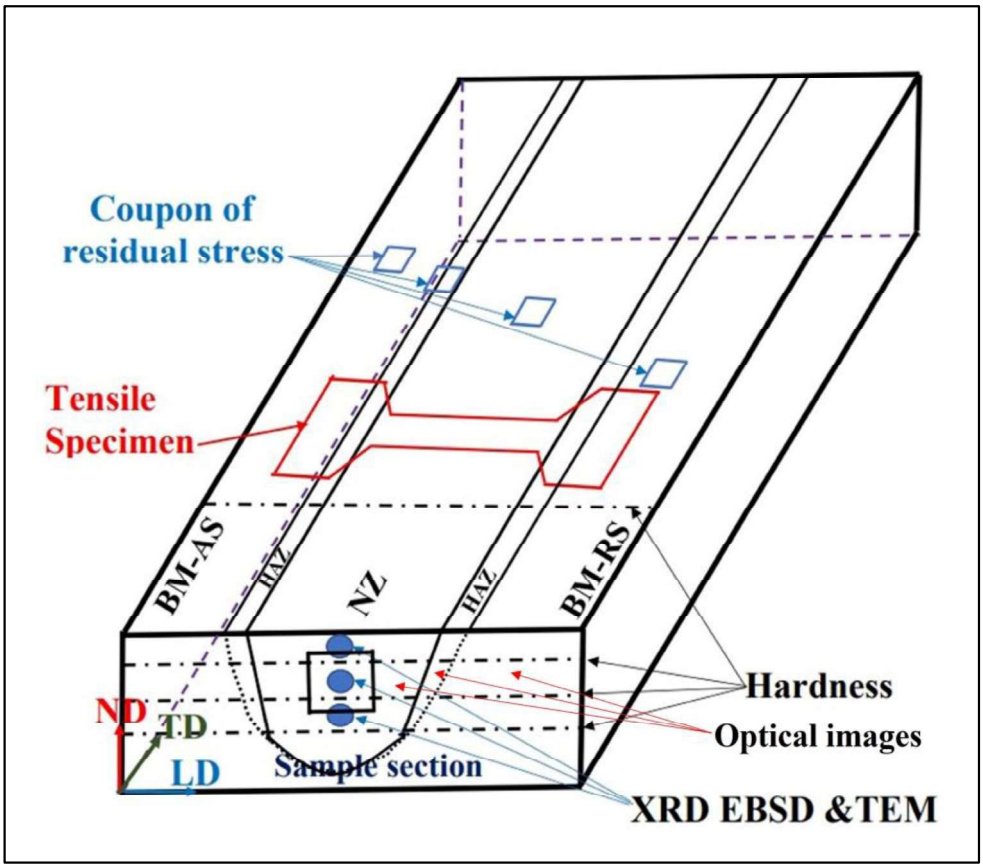

Fig. 2.6. Schematic diagram of the friction-stir processed plate: the location of specimens for various characterization is displayed, LD, TD, and ND represent the longitudinal, transverse, and normal directions, respectively, BM, AS, and RS, are base-metal, advancing and retreating sides. NZ, and HAZ, depict serially the nugget zone and heat-affected zones.

2.7 Structural and microstructural characterization

The optical microscope characterizes microstructural features using visible light. This is also suitable for large-scale observations of the microstructure. X-ray diffraction is used to identify the crystal structures, measure lattice micro-strain, crystallite size, and dislocation density, and detect the various metastable phases formed during the age-hardening techniques. HR-XRD is used to analyze the crystallographic properties of the alloys. It provided detailed information on the crystal structure, lattice parameters, and crystallographic orientation, for instance, the bulk texture characterization (pole figure (PF) and orientation distribution function (ODF)), and residual stress is analyzed using the 3D-

scanning (Chi, Omega, 2θ) with the help of point scanning. Scanning electron microscope (SEM) examines the surface topography and morphology of the fractured specimens. This is also useful for visualizing the microstructural features at relatively high magnifications. SEM-EDS elemental mapping (point and area) determines the chemistry of phases using the x-rays emitted from the sample surface. Electron backscattered diffraction (EBSED) is used to study the micro-texture characteristics of the materials. The technique involves collecting the backscattered electrons from the sample surface. This provides information about the crystallographic orientation (grain size, misorientation angle, IPF map, and image quality (IQ, CSL boundary). The transmission electron microscope (TEM) is used to obtain the structural and microstructural features at the atomic scale (Å, level). This also enables the observation of the thin section of the specimen. High-angle annular dark field (HAADF) STEM imaging analyses the chemistry of different phases. The technique involves detecting the high-angle scattering of the electrons, resulting in the dark background of the images. By detecting variations in the atomic numbers, the technique could also reveal the compositional differences. HRTEM gives high-resolution images up to the atomic level. This could also reveal the arrangement of the atoms and the lattice fringes in the crystal structures of the alloys. The fine details of atomic structures and the defects present inside the alloys are also determined with the help of HRTEM imaging. The detailed working principle of each characterization technique and the co-related sample preparation techniques are given below:

2.8 Optical microscopy

An optical microscope, also known as the light microscope, is a widely used instrument for magnifying small objects which is not visible with the help of the naked eye. The major function of the microscope relates to illuminating the sample, magnifying it, resolving the features, generating a contrast and finally capturing the display images. Its working principle

is based on the interaction of visible light with the sample, allowing for the visualization of details and structures in the microscale. It has three major components: 1. The eyepiece, 2. The light source, and 3. Objective lenses (a series of glass lenses). The microscope uses a visible light source which illuminates the specimen. The condenser lens helps to control and focus the light coming from the light source. By suitable adjustment of the condenser lens, one may regulate the amount and intensity of the light. The sample could be mounted on the sample stage between the objective lens and the condenser lens. The objective lens plays a crucial role in magnifying the sample. The light rays coming from the different points on the sample diverge and enter the objective lens, which focuses the rays to form real and magnified images. A series of lenses or the so-called tube lens further magnifies the intermediate image created by the objective lens. Therefore, the combination of the objective lens and a series of tube lenses is responsible for getting the total magnification of the object. The eyepiece which is located on top of the optical microscope also contains the lenses which further magnify the object during the optical micrographic examination. The schematic details of the optical microscope are given in Fig. 2.7.

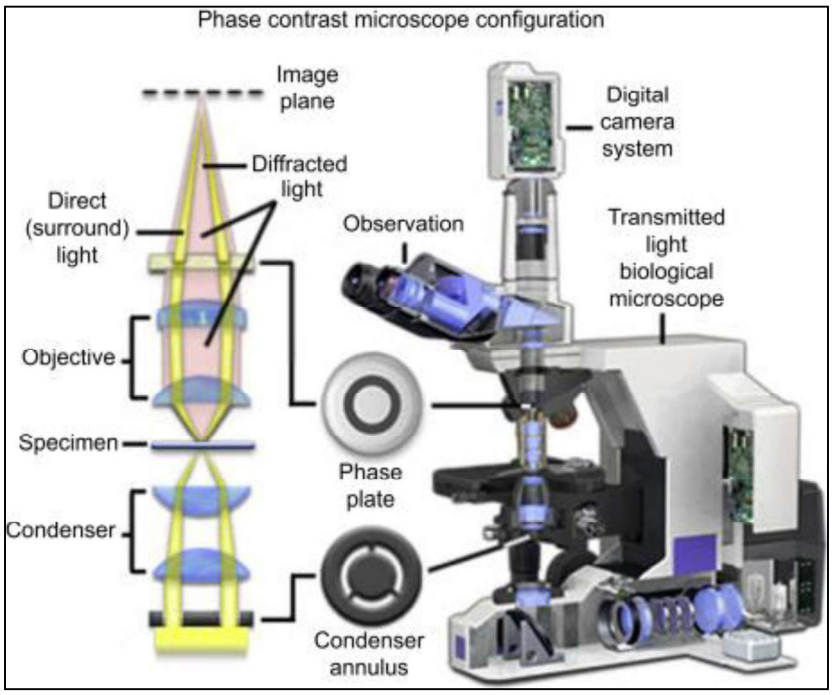

Figs. 2.7 Schematic of the optical microscope: showing the visible light source, objective, and condenser lenses [141].

Specimens for optical microscopy are prepared from the base metal and friction stir processed samples. These are mechanically polished using 1000, 1500, and 2000-grade emery papers. Final polishing was carried out with the help of 3μm and 1μm grade papers. The diamond suspension (1μm), and colloidal silica (0.05μm, 8.5 pH) are also incorporated as a polishing agent. The polished samples are etched with the help of Keller's (2ml HF, 3ml HCl, 5ml HNO_3, 190ml H_2O) at room temperature (25ºC). Microstructures are examined using the Leica (OM,) at 100, 200, and 500 magnifications.

2.9 X-ray diffraction

X-ray diffraction (XRD), is a process involving the focused and single-wavelength X-ray beam in the samples. The X-ray provides constructive interference-assisted diffraction which is observed at a particular angle (represented by θ) and corresponds to the specific crystal

planes. The crystal planes exhibited a particular condition where differences in the path travelled by the diffracted rays are equal to the integer multiple *(n)* of the X-ray wavelength. The Bragg's condition given in Eq. 2.1, generally describes Bragg's law of X-ray diffraction.

The Bragg's law: $n\lambda = 2dSin\theta$…….*Eq. 2.1*

Here, λ = wavelength of the incident x-ray beam, d = inter-planar spacing, θ = scattering angle, and n = integer-called the order of diffraction.

For analyses of the crystal structures in metals and alloys, the X-rays are diffracted by oriented crystallites at a particular angle to satisfy Bragg's condition. Having known the value of θ, and the λ one may calculate the inter-planar spacing (d, in Å) value. The XRD can be used in different modes such as θ-2θ scanning geometry, and Bragg's Brentano geometry. In the θ - 2θ, geometry, the monochromatic x-ray beam is incident on the sample surface at an angle of θ, and the detector motion is coupled with the x-ray source such that it always makes the angle 2θ corresponding to the incident direction of the x-ray beam as displayed in Fig. 2.8.

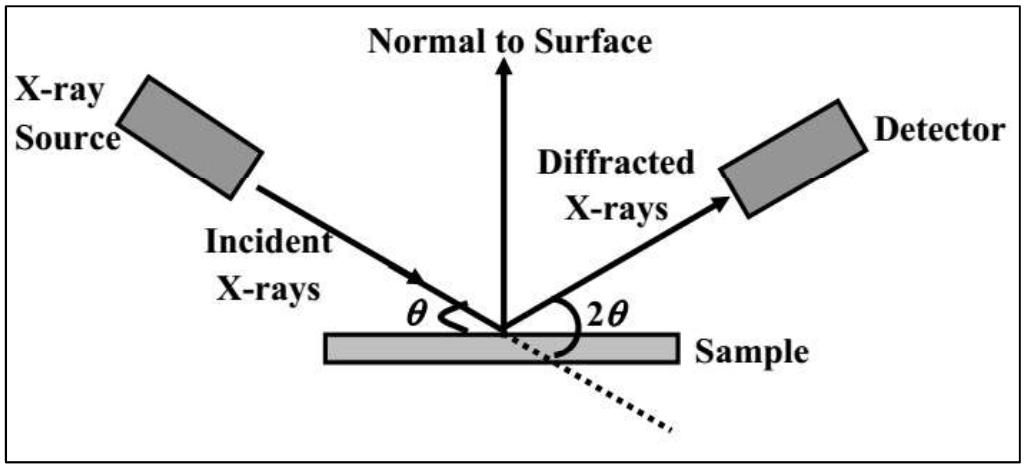

Fig. 2.8 Schematic of the working principles of the X-ray diffraction (*θ-2θ* geometry)[142].

XRD investigation of the heat-treated (T4, T6, T73, and T7352), thermo-mechanically processed (TMP-1, TMP-2, and TMP-3), and friction stir processed alloys were done with the help of *Rigaku MiniFlex 600 XRD* (λ= 1.54Å) at the operating voltage of 40kV and 15mA, and the *PANalytical Empyream MRD* system using the Co Kα radiation (*λ = 1.67Å*), at the operating voltage of 40 kV and 40 mA. The geometry of the former (Rigaku Mini Flex 600 XRD) is related to the θ-2θ geometry, while the latter (*PANalytical Empyream MRD* system) is based on Bragg's Brentano geometry. For XRD analyses, the metallographic sample preparation (*10mm x 10mm x 3mm*) was done following the standard metallographic sample preparation technique. For instance, grinding, and mechanical polishing with the help of 1000, 1500, and 2000 grade emery papers followed by the cloth polishing using the Brasso solution. The samples from the heat-treated, and thermo-mechanically processed alloys are extracted keeping the rolling direction *(RD)* parallel to the sample direction of the alloy. However, the FSP samples are extracted keeping the normal direction and the processed direction of the specimens parallel as shown in Fig. 2.6. All the specimens are scanned within the angular range *2θ* of ~10º to 90º for Cu Kα (*λ=1.54Å*) source. On the other hand, 15º to 100º for the Co Kα (*λ= 1.67Å*) source. For bench-top XRD (Rigaku MiniFlex 600) the specimens were wrapped inside a cello-tap and held inside the circular aluminum holder, in such a way that the top surface of the specimen was to be exposed to an X-ray source. All the samples were loaded horizontally and kept side-by-side on the specimen stage equipped with the six slots. The HR-XRD sample is individually loaded on the sample stage before the XRD investigation. The analysis of the XRD pattern is done with the help of the JCPDS/ ICDD data cards.

2.10 Bragg's Brentano geometry

Phase analyses, and bulk texture measurements of the thermo-mechanically processed (TMP-1, TMP-2, and TMP-3) alloys are done using the *PANalytical Empyrean MRD* system with the help of *Bragg's Brentano geometry*. The geometry is designed in such a way that it could enhance the intensity of the diffraction peaks. This is achieved by positioning the X-ray or neutron source, the sample, and the detector in a specific way to optimize the diffraction process. To obtain such geometry a monochromatic X-ray or neutron beam (single wavelength) is generated in the specific operating voltage and current of the 40kV, and 40mA, that is directed in the samples for accurate diffraction measurement. The crystalline sample is placed in the path of the X-ray beam. The crystal lattices of the specimen cause the incident X-rays to be diffracted at specific angles and give the diffraction pattern. The crystal lattice spacing (d-spacing), and the incident angle determine the diffraction angle at which these patterns will occur. A goniometer is a device that allows precise rotational control of the sample and the detector. In this specific geometry, the sample is rotated while keeping the detector fixed at a specific angle relative to the sample to ensure that the diffraction conditions are met at all times. The detector is positioned at a fixed angle, usually at twice the angle of the incident beam with respect to the sample. These configurations allow the diffracted X-rays to be collected over a wide range of diffraction angles. As the sample is rotated, the diffracted X-rays hit the fixed detector at different angles. The intensity of diffracted X-rays at each angle is measured, resulting in a diffraction pattern, which gives information about the crystal lattice structure and the arrangement of atoms within the sample. The schematic details of the sample geometry are given in Fig. 2.9.

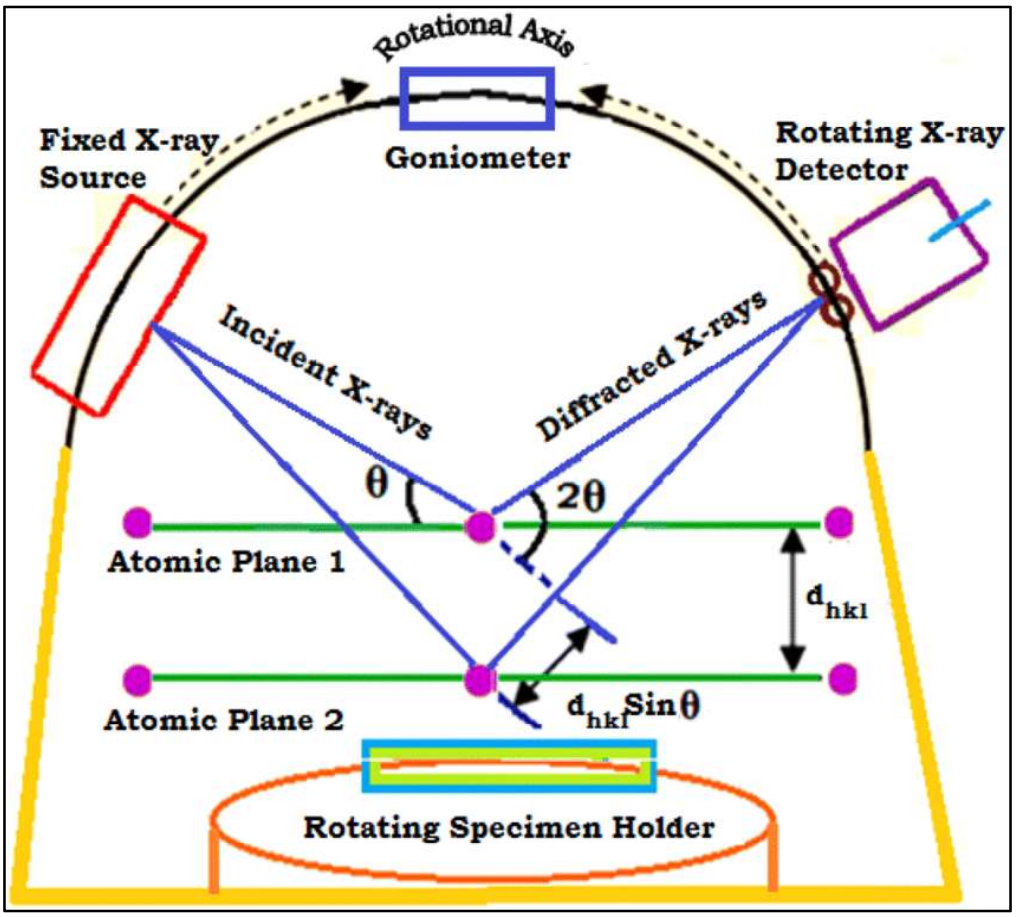

Fig. 2.9 Schematic of the working principles of the X-ray diffraction (Braggs Brentano geometry) [142].

2.11 Lattice micro-strain *(ε)*, crystallite size *(D in Å)*, and dislocation density *(ρ/m^2)* calculation using the XRD raw data

The XRD data can also be utilized to determine various parameters attributed to the lattice structure, crystallite size, micro-strain within the lattice, and dislocation density. The stepwise measurement procedures are given below:

To ascertain the size of individual crystallites (D_{hkl}), and the residual lattice micro-strain within the lattice (e_{hkl}), we focus on the major XRD peaks of α-Al, specifically the (111), (220), and (311) planes. These values are extracted from the corrected Lorentzian and

Gaussian components of the integral breadth widths. The corrected Lorentzian components (denoted as β'_L) for each plane are separated from the instrumental breadth using Eq. 2.2.

$$\beta'_L = \beta_L - \beta_{L0} \quad \text{Eq. 2.2}$$

Here, β_{L0} represents the instrumental breadth for the respective 2θ of the α-Al reflecting plane. It is determined by putting the 2θ value into a polynomial equation obtained from a second-order polynomial fitting using 2θ vs. β_L data for all major reflecting planes of the standard Si crystal. The β_L value is the Laurentzian component of the integral breadth of the respective 2θ of the α-Al reflecting plane. Similarly, the corrected Gaussian component (β'_G) of the integral breadth is extracted from the Gaussian component (β_G) using *Eq. 2.3.*

$$\beta'^2_G = \beta^2_G - \beta^2_{G0} \quad \text{Eq. 2.3}$$

Here, β_{G0} denotes the instrumental breadth for the respective 2θ of the α-Al reflecting plane, which is obtained in a similar way as the β_{L0} was obtained.

The crystallite size (D_{hkl}) for all planes (111, 220, and 311) and lattice micro-strain (e_{hkl}) are calculated using *Eq. 2.3* and *Eq. 2.4*, respectively:

$$D_{hkl} = 0.91\lambda / (\beta'_L * \cos(\theta)) \quad \text{Eq. 2.4}$$

$$e_{hkl} = \beta'_G / (4 * \tan(\theta)) \quad \text{Eq. 2.5}$$

In these equations, θ represents Bragg's angle, D is the crystalline size, and λ is the wavelength of the X-ray radiation.

Further, the dislocation density at the (hkl) planes is determined using the crystallite size and the lattice micro-strain based on the crystallite size and the lattice micro-strain using Eq. 2.6.

Dislocation density:

$\rho_{hkl} = 2\sqrt{3} * \sqrt{(e^2_{hkl})} / (D_{hkl} * b)$ ……..*Eq. 2.6.*

Here, b represents the Burger vector for α-Al, which is approximately 2.85 Å.

2.12 Residual stress, and bulk texture measurement (HR-XRD data)

The thin specimens of *10x10 mm*^{2} cross-sectional area and 3 mm thick are extracted from the nugget zone (N.Z.), heat-affected zone (HAZ), and base-metal (B.M.) of the processed sheet along the longitudinal direction. Samples are ground and polished. The polished samples are positioned in the middle of the holder such that the transverse direction of the friction stir processed specimen is parallel to the Chi (χ) axis and the normal direction of the sample is parallel to the phi (ϕ) axis. Samples are scanned in point focus mode. Three-dimensional angular-scanning is made, respective to the **Incident angle, Omega (ω):** {range: 4.0, step size: 0.04, and time per step: 0.3 sec}, **Diffraction angle 2θ**: {range: 1.0, step size: 0.01, and 0.3 sec/ step time}, **Rotation angle, Chi (χ): {**range: 1.0, step size: 0.01, time/ step: 0.3 sec }, **Offset angle Psi (ψ)**: (max limit 12 and step size of $\sin^2\psi$ of 0.4), and the scanning for Z-height adjustment are done, at 40 kV, and 20 mA. After successful angular scanning, and height adjustment, the beam attenuator and parallel plate collimator slit are removed, and Fe(β) filter for the Co source is inserted. High angle peak position, 2θ of a higher count, is selected from the phase analysis data. Gonio scanning {range: 4.0, step size: 0.05, and time per step: 1sec} is performed to review the scanned peak. Full-width half maxima (FWHM) of high-angle scanning peaks are determined, which is divided by the two-numerical values 10, and 6, respectively, and the step size is selected within these values. The step size and time per step are decided so that the number of steps falls between 100 and 120. Finally, all the scanning for residual stress measurement is done with the help of the *PANalytical Empyrean MRD*- system with *Co-Kα* radiation, using the Chi-square (χ^2) method at 40 kV

and 40 mA power supply. After successful scanning, residual stress is calculated with the help of X'Pert stress software. The d-spacing values are computed for various ψ tilts. The inter-planar spacing (d, in Å) vs $Sin^2\psi$ are plotted. For the bulk texture analysis three-dimensional scanning respective to **Incident angle, Omega (ω):** {range: 4.0, step size: 0.04, and time per step: 0.3 sec}, **Diffraction angle 2θ**: {range: 1.0, step size: 0.01, and 0.3 sec/ step time}, **Rotation angle, Chi (χ):** {range: 1.0, step size: 0.01, time/ step: 0.3 sec }, **Offset angle Psi (ψ)**: (max limit 12 and step size of $sin^2\psi$ of 0.4), and the scanning for Z-height adjustment are done, at 40 kV, and 20 mA. After successful angular scanning, and height adjustment, the beam attenuator and parallel plate collimator slit are removed, and Fe(β) filter for the Co source is inserted. Phase scanning of the bulk solid crystalline sample is done in the range of 2θ~20º to 90º sections. The texture scanning is done respectively to the high intensity 2θ peak positions of 45º, 54º, and 68º for the α-Al cF4 structures.

The pole figure data respective to high-intensity peaks are recorded. With the help of the three pole figure data, the ODF is calculated.

2.13 Bulk texture

Any preferred orientation of the polycrystalline aggregates is known as the texture. Bulk texture, also known as macro-texture, provides information about the density and volume fraction of any given orientation, which is prevalent in the microstructures that constitute the texture. However, it does not furnish any specific details about the spatial location of those orientations in the microstructure. The bulk texture is generally represented by pole figures (PFs) and orientation distribution functions (ODFs). Bulk textures are generally measured by X-ray or neutron diffraction.

2.14 Bulk texture measurement

This could be measured with the help of the pole figure and the orientation distribution function

2.14.1 Pole figure

Orientation of the crystallite is presented with the help of pole figures, which are modified forms of the stereographic projection. A stereogram is a representation of the 3D unit cell in a 2D plane, whereas a pole figure displays the stereogram of a polycrystal with a sample frame of reference embedded. The difference between the pole figure and the stereogram is given in Fig. 2.10.

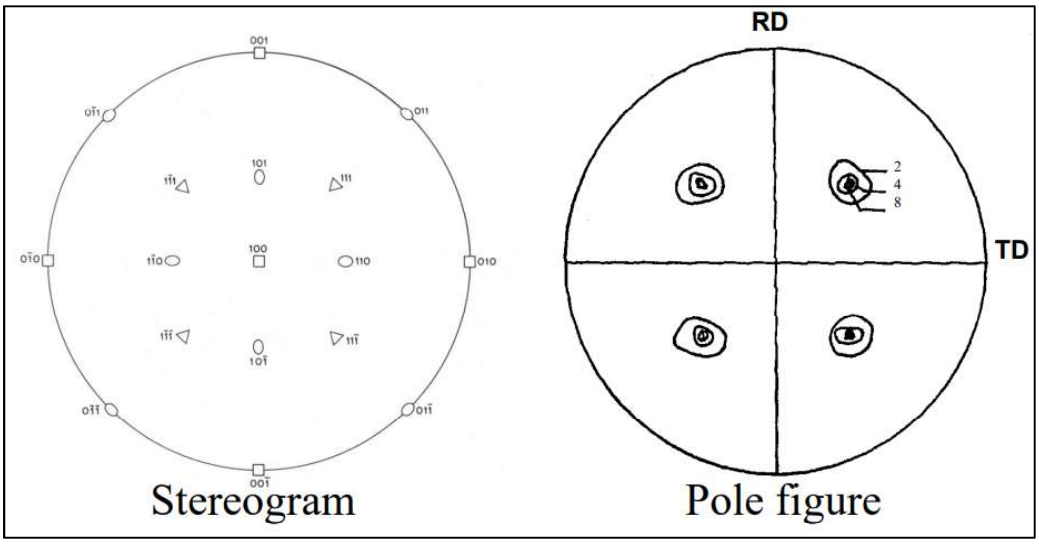

Fig. 2.10 Difference between the stereogram and the pole figure: (a) stereogram and (b) pole figure [110].

2.14.2 Inverse pole figure (IPF)

The technique involves mapping the crystal axes in a single stereographic triangle. In this, the specimen reference frame (RD, TD, and ND) is projected in the crystals reference frame (100, 010, and 001), in reverse of the Pole figure, where crystal reference frame (100, 010, 001) is projected on the specimen reference frame. Such visualization technique is termed

an inverse pole figure (IPF). The texture of materials subjected to processes like extrusion, wire drawing, and compression are effectively described with the help of IPF. This also becomes important to illustrate the texture of uniaxially deformed materials. To study the texture of the thin films IPFs become important, where only the sample plane's normal direction needs to be represented to show the texture of the thin films. The IPF map for the wire-drawn axis is shown in Fig. 2.11.

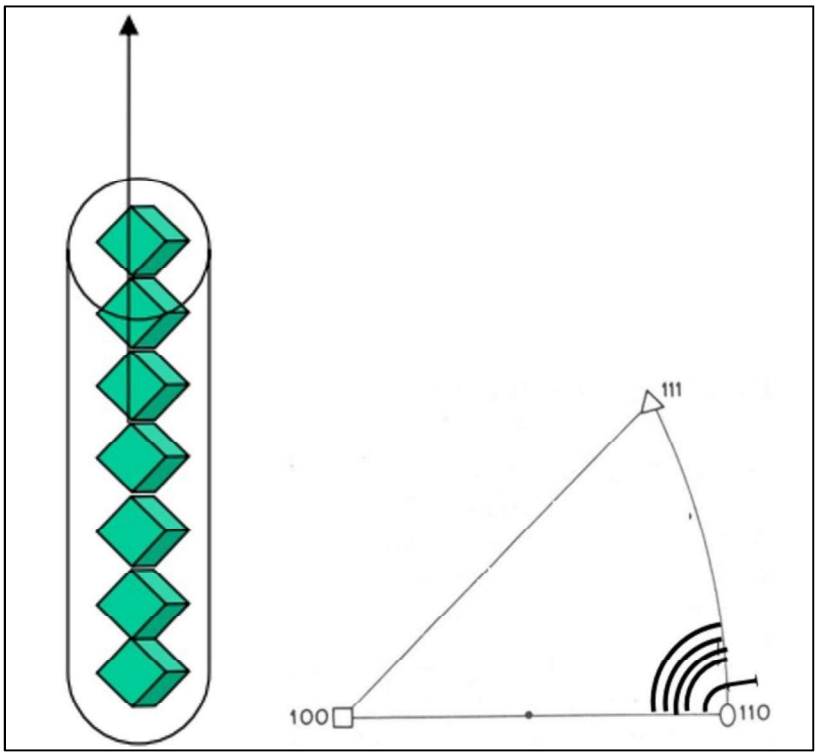

Fig. 2.11 Wire-drawn axes and respective IPF, orientation contour will form near 110 in IPF [110].

2.14.3 Orientation distribution function (ODF)

ODF is a mathematical function that depicts the frequency of occurrence of particular crystal orientation in 3D Euler space, whose coordinates are defined by the three Euler angles (Φ_1, Φ, Φ_2). These angles are obtained after three consecutive rotations which need to be given to each crystallite in the specimen to bring its crystallographic axes (100, 010, and 001) into co-incidence with the specimen reference frame (RD, TD, and ND). The texture of the single

crystal polycrystalline material is represented by the ODF, which represents the volume fraction of the crystallites having orientation of crystal axis with reference to a fixed coordinate system (RD, TD, and ND).

By volume, texture could be described as:

The $dv(g)/V = f(g)\, d(g)$ ……..*Eq. 2.7*

By number, ODF is given as:

$dn(g)/N = f(g)d(g)$…… ……..…….*Eq. 2.8*

The $d(g) = 1/ 8\pi^2 \text{Sin}\Phi\, d\Phi\, d\Phi_1\, d\Phi_2$…….……..…...*Eq. 2.9*

Here, "g" is the parameter of orientation = $[g_{ij}]$, $\{\Phi_1, \Phi, \Phi_2\}$ is the Euler angles, and (hkl) <uvw> is the crystal direction.

For the quantitative texture characterization, one needs to understand the orientation of the crystal in the polycrystalline aggregates. The orientation of polycrystalline aggregate could be described as the relationship between the crystal reference frame and the specimen reference frame, which is given below:

$$Cc = \Phi\, Cs \text{ ……..*Eq. 2.10*}$$

Here, Φ (Φ_1, Φ, Φ_2, Bunge notations) denotes the orientation of the crystal in a polycrystalline aggregate, which when performed rotations in a correct sequence coincides with the crystal reference (Cc) frame with the specimen reference frame (Cs). The specimen coordinate system could be described as RD TD and ND whereas the cubic crystal axes are given by 100 along the X-direction, 010 along the Y-direction, and 001 along the Z-direction of the cubic crystal system.

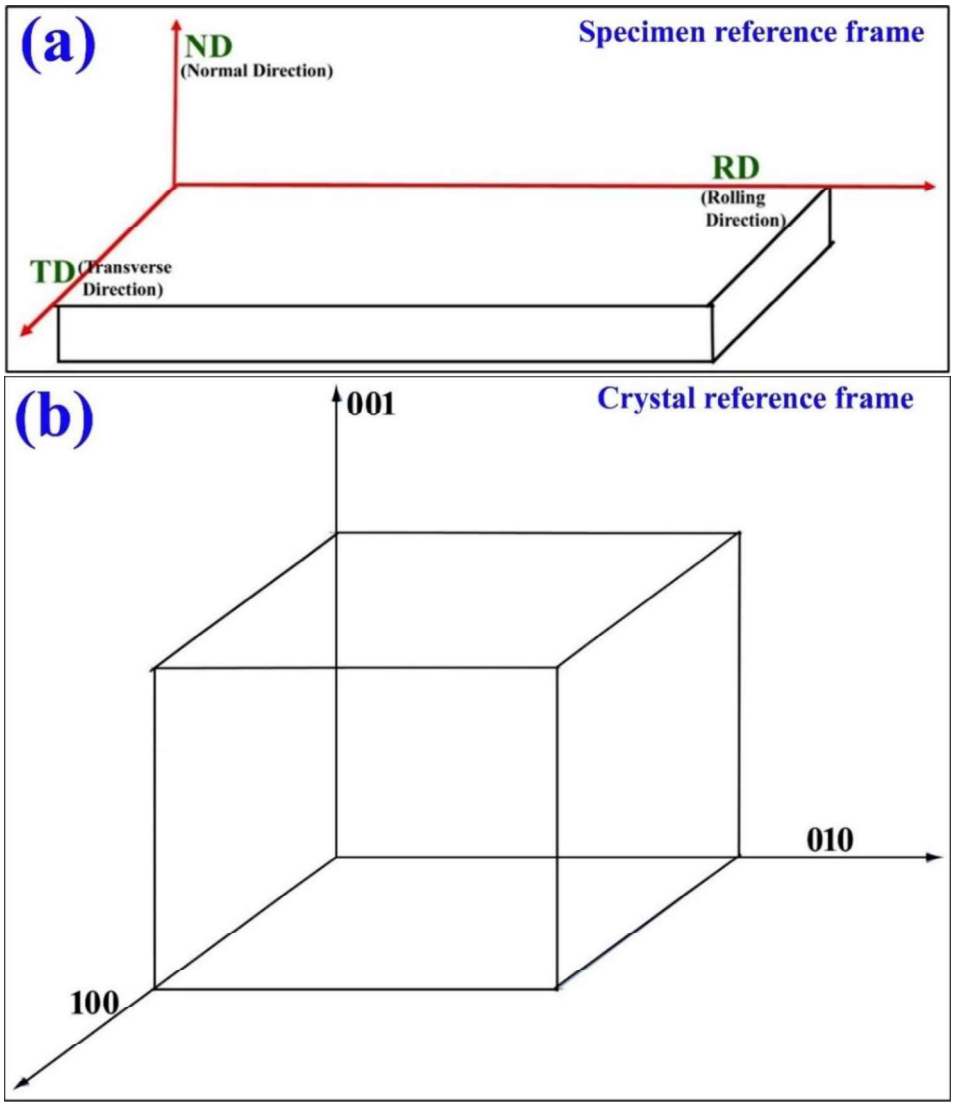

Figs. 2.12a-b Schematic of the specimen reference frame and the crystal reference frame: (a) specimen reference frame, RD = rolling direction, TD= transverse direction, and ND = normal direction, (b) crystal reference frame: 100, 010 and 001 display three axes of the crystal orientation.

2.15 Scanning electron microscope

Scanning electron microscopy (SEM) is a technique within electron microscopy that finds extensive application in the field of diverse materials characterization such as metals, ceramics, and polymers. Its primary objective is to analyze the material's features like surface morphology, fracture surface, and elemental distribution (both in lines and areas).

The utility of SEM extends to investigating the surface texture, topography, particle size distribution, and chemical composition. The insights furnished by SEM predominantly concern the outermost layers and immediately underlying regions of the specimen.

The major components of the SEM apparatus encompass a vacuum chamber, an electron gun, condenser lenses, an objective lens, a sample chamber, detectors, and a sample stage, as shown in Fig. 2. 13a. On the other hand, the arrangement of the SEM along with its signal detectors is displayed in Fig. 2.13b.

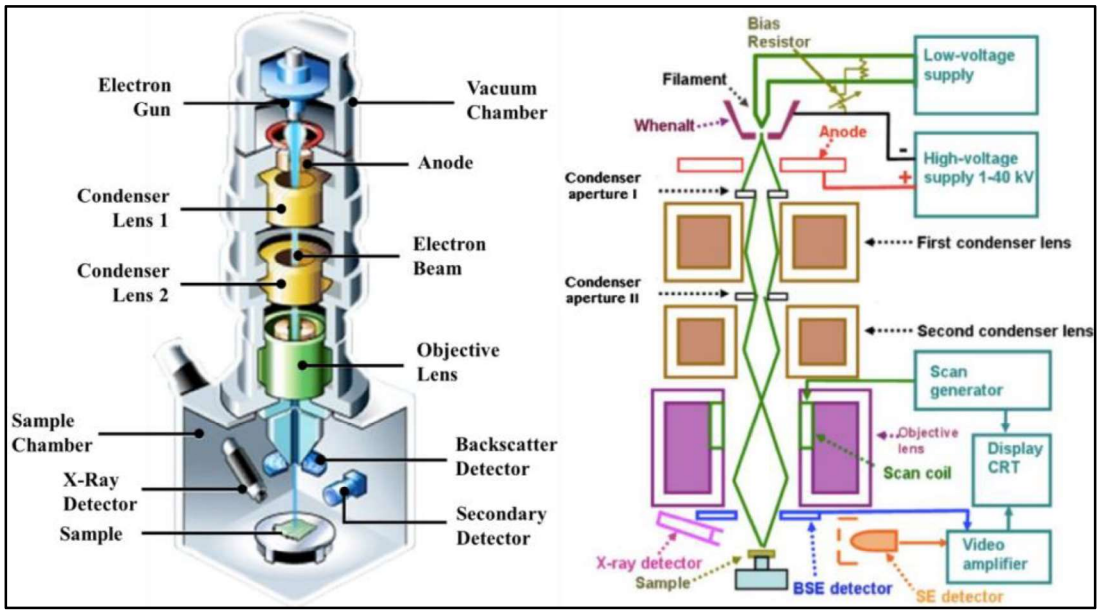

Figs. 2.13a-b Schematic of SEM: a) Front half section, b) Electron beam trajectory [141].

The electron gun serves as the main source of an electron beam, carrying energies ranging from a few hundred electron volts (eV) to a few kilo-electron volts (keV). This high-energy electron beam scans the sample surface with the aid of the scan coils, facilitating a comprehensive examination. Furthermore, the high-energy electron beam penetrates the sample surface to a depth of a few micrometers, thereby leading to interactions between the electrons and the specimen. These interactions could be categorized as elastic or inelastic by

nature. Based on these interactions, a variety of valuable signals are generated, including the Auger electrons (AEs), Secondary electrons (SEs), X-rays, Backscattered electrons (BSEs), Characteristics X-rays, Continuous and fluorescent X-rays, which are given in Fig. 2.14.

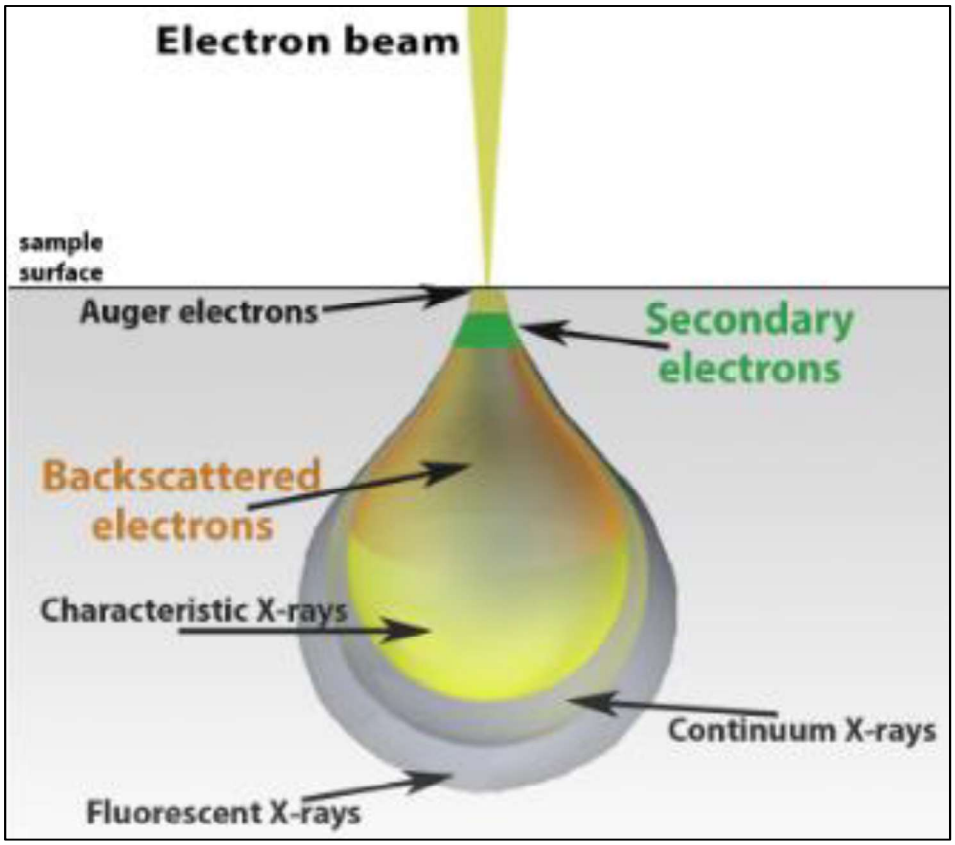

Fig. 2.14 Emission of electrons from the sample surface, while specimen-electron interaction [141].

2.15.1 Emission of electrons from the sample surface and their significance

Backscattered electrons are a product of elastic interactions and exhibit reflection from the material's surface with higher energy. This property enables easy differentiation of contrast in backscattered electron images by leveraging the atomic numbers of the constituent elements. Conversely, secondary electrons are discharged from a shallow depth (a few nanometres) below the specimen's surface due to the inelastic interaction between the electron beam and the specimen. Secondary electrons possess lower energy compared to the

backscattered electron. In scanning electron microscopy, an X-ray is produced when an electron beam displaces an inner shell electron, which is then replaced by the outer shell electron. Because each element has a distinct energy difference between the outer and inner electron shells, the X-rays observed provide an elemental identification. EDS data can be acquired at a single spot, coupled with a line, or mapped over an area. The differentiation observed in the backscattered electron image results from the combination of factors. These include the specimen's atomic number (Z), the energy at which the primary beam is accelerated, and the angle at which the specimen is tilted relative to the primary beam. Elements within materials that possess a higher atomic number (Z) contribute more to the emission of the backscattered electrons in comparison to those with lower atomic number (Z) values

2.15.2 Micro-texture characterization (using EBSD in SEM)

Microtexture encompasses both crystallographic parameters and microstructure attributes, including features like morphology, size distribution, shape, crystal orientation, and their relationship with each other. Essentially, microtexture combines microstructure with crystallographic orientation, offering a means of analyzing the spatially resolved aspects of a material's microstructure. This spatially resolved microstructural analysis serves as a consistent method for characterizing microstructural properties and determining their crystallographic orientations. Assessing micro-texture involves a single-grain approach, yielding a diffraction pattern from each sampled volume. Typically, micro texture determination relies on techniques like SEM and TEM, which account for the formation of the Kikuchi patterns.

2.15.3 Measurements of micro-texture

Micro-texture analysis relies on individual grain-based techniques, with the primary outcome being the generation of diffraction patterns from each sampled volume. These patterns encompass crystallographic data alongside the orientation specifics of the sampled volume, which is essentially a discrete crystalline entity with uniform orientation. Various techniques are available for micro-texture determination, including **1.** Selected Area Channelling (SAC) in SEM, **2.** Electron Backscattered Diffraction (EBSD) in SEM, and **3.** Microdiffraction or Convergent Beam Electron Diffraction (CBED) in the TEM. Among them, EBSD stands out as the most commonly employed approach for micro-texture analysis and is effectively executed through EBSD technology.

2.15.4 Electron backscattered diffraction (EBSD)

Proper sample preparation is crucial for obtaining accurate and reliable results in EBSD analysis. For this purpose, metallographic samples are prepared using standard metallographic techniques. The specimens with dimension: *10mm (length) x 8mm (width) x 4mm (thick)* are extracted from all the heat-treated (T4, T6, T73, and T7352), thermo-mechanically processed (TMP-1, TMP-2& TMP-3), and friction-stir-processed (FSP1000-1P, FSP1000-2P& FSP1000-3P, FSP+PA, SQ+FSP+PA) alloys. The samples are ground and mechanically polished using the colloidal silica and diamond paste. Thereafter, electropolishing is done with the help of 10% HNO_3+90% CH_3OH at 20V and 5ºC temperature. The electropolished sample was kept in the sample holder. The samples are automatically tilted to 70º, thereafter EBSD scanning for all the samples is done with the help of an EBSD detector attached to the scanning electron microscope (SEM, FEITM-Quanta 3D FEG) operated at 30kV. The step size (0.2 μm) and scanning area (150x150 μm^2) are kept constant for the measurement. The microstructural features, for instance inverse

pole-figure (IPF) map, grain-size determination, and the misorientation angle measurement, are done using the EBSD data with the help of TSL OIMTM software (version 8.0). Grain boundary characteristics are defined in the following manner, a misorientation angle between 2-15° is denoted as a low-angle grain boundary. In contrast, a misorientation angle of more than 15° is defined as the high-angle grain boundary. All the edges of the specimens were made perpendicular to each other as shown in the sample geometry in Fig. 2.12b. The RD, TD, and ND are made perpendicular to each other. Automated Electron Backscatter Diffraction (EBSD) has evolved as an advanced method for quantitative texture analysis, serving as an alternative to X-ray pole figure measurements. Unlike X-ray methods, automated EBSD overcomes challenges like ghost artifacts, defocusing issues, and inconsistent data caused by extensive specimen tilting. This automated technique has introduced fresh possibilities in quantitative texture analysis due to its remarkable spatial resolution, access to orientation correlations and stereology, rapid processing speed, and the capability to visually and quantitatively portray texture and grain boundary characteristics through orientation maps. In EBSD, a stationary electron beam is directed onto the selected region of the specimen, generating a Kikuchi pattern. The spot size, which defines the region where the primary beam interacts with the crystal to form the Kikuchi pattern, can be significantly reduced compared to older methods. This enhanced control over the interaction volume enables a spatial resolution two orders of magnitude finer than what's achievable with traditional Electron Channelling Patterns (ECP). The spatial resolution, as well as the depth resolution in EBSD, is influenced by factors like specimen tilt, specimen density, and the accelerating voltage used.

2.15.5 Components of the EBSD

An automated EBSD system consists of three main parts: the SEM, the pattern acquisition device (or camera), and the software. To achieve the best possible performance, these parts must be considered simultaneously when designing and setting up a system. Significant effort is necessary to ensure the coupled system works synchronously and to develop complex software for controlling the SEM functions, pattern acquisition, and data interpretation. The following intrinsic difficulties of EBSD must be addressed: 1. Steep specimen tilt, approximately 70◦ relative to the incident beam. 2. Low contrast and intensity, and high background noise in the backscatter Kikuchi patterns. 3. Disposition to pattern degradation by contamination and deformation layer. The schematic of EBSD geometry is given in Fig. 2.15.

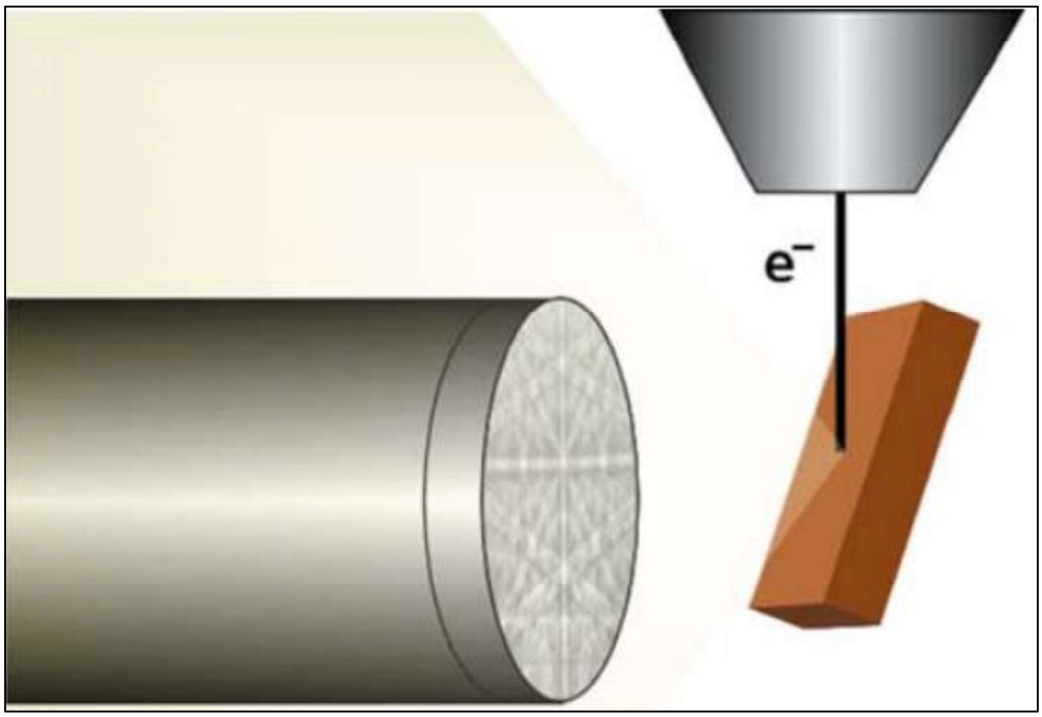

Fig. 2.15 Schematic of the typical EBSD geometry showing the Pole piece of SEM, the electron beam, the tilted specimen, and the phosphor screen [112].

2.15.6 Formation of Kikuchi Patterns

When an electron interacts with a crystalline solid, it scatters in various directions. Kikuchi lines form due to the inelastic scattering of electrons, leading to Bragg diffraction at the particular point (S) on the lattice planes with indices hkl. At each set of these lattice planes, electrons arrive at the Bragg angle, and these electrons can experience elastic scattering, resulting in a strong, intensified beam. Because electron diffraction takes place in all directions, the path of diffracted radiation forms a cone's surface. This cone extends outward from the normal to the reflecting atomic planes, with a half apex angle of 90º minus θ. We can envision the source of electron scattering as being located between the lattice planes, resulting in the generation of two radiation cones for each family of planes. The origin of electron scattering can be thought of as situated between the lattice planes, leading to the generation of two radiation cones stemming from each set of planes in the family. The schematic details of formation of the Kikuchi patterns in SEM are given in Figs. 2.16a-d

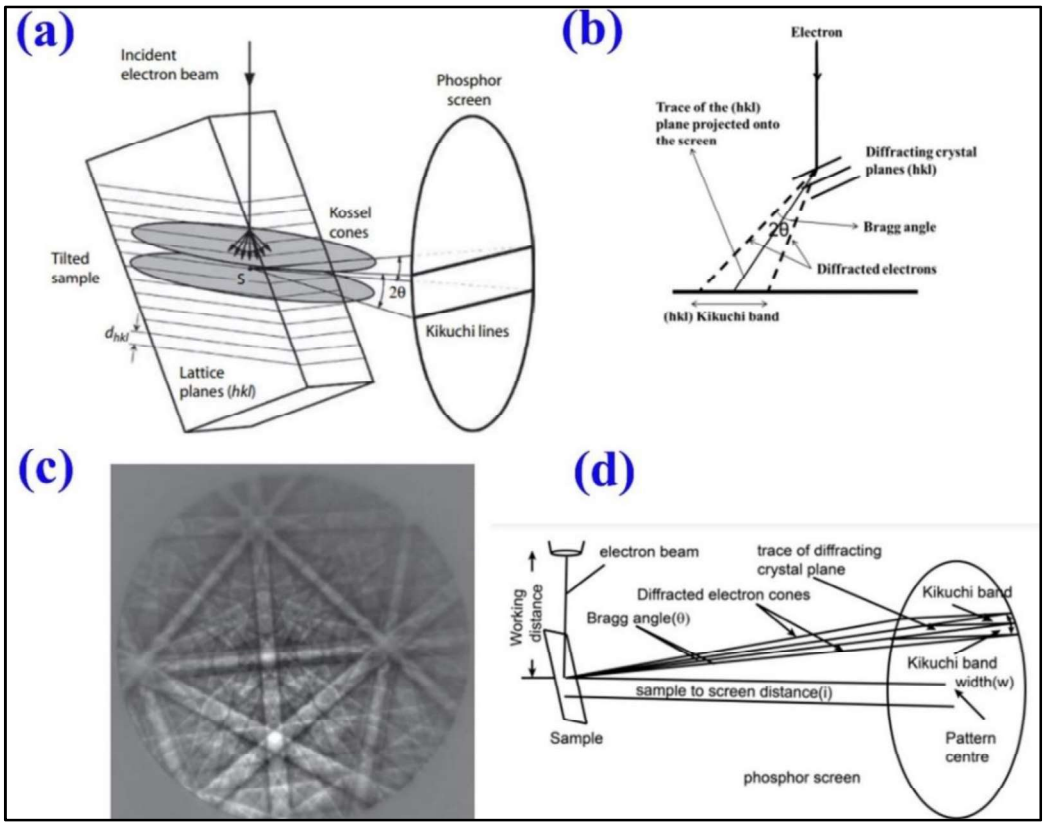

Figs. 2.16a-d Formation of the backscattered Kikuchi patterns by EBSD in SEM: (a) origin of the Kikuchi lines from the EBSD, (b) EBSD pattern from the Cu, cubic f.c.c. (c, d) Schematic details of the formation of the Kikuchi patterns in SEM EBSD for the single electron beam [112].

2.15.7 Bright and dark Kikuchi lines

TEM Kikuchi patterns usually consist of pairs of bright and dark lines, which means that an offset must be introduced when determining the background intensity to ensure that the defect Kikuchi lines with intensities below that of the background are not removed. In contrast, EBSD patterns mainly comprise bands with a higher intensity than their surroundings, and only occasionally sharp, bright, and dark lines are observed at the band edges. Furthermore, low-index lines in TEM are frequently associated with parallel high-order diffraction lines. The interpretation of Kikuchi patterns comprises two essential stages:

1. Identifying the crystallographic indices associated with the Kikuchi bands or the relevant

lattice planes, and 2. Establishing the relative positioning of these bands or poles concerning an external reference frame. Qualitative information could also be obtained by suitable observations of the Kikuchi patterns. For example, lattice strain can be recognized through the blurring or spread observed in the diffraction pattern, resulting from the bending of lattice planes. The grain or phase boundaries can be detected by observing alterations in the live diffraction pattern as the sampling probe moves across the specimen surface. With practice, one can perform tasks like distinguishing between low-angle and high-angle boundaries, assessing the integrity of individual crystals, or approximating the distribution of grain sizes. Some orientations, such as the cube orientation $\{001\}\langle 100\rangle$, can be quickly recognized through visual inspection, aided by superimposing a computer-simulated diffraction pattern that corresponds precisely to the target orientation onto the live patterns.

2.16 Structural characterization

Structural investigations of the heat-treated (T4, T6, T73, and T7352), cold deformed (TMP-1, TMP-2, and TMP-3) followed by the peak-aging (T6, aging at 120ºC, for 24hrs) and friction stir processed (at 1000rpm, FSP+PA, SQ + FSP + Peak-aged) alloys are done with the help of transmission electron microscope operated at 200kV/ 300kV. For this 0.6 mm thin specimen is extracted from all the heat-treated, cold-deformed, and friction-stir-processed specimens. After that the specimens are thinned down to 50 to 70 µm thickness, using the 320 and the 1000 grade emery papers. The 3mm diameter thin slice is punched from the mechanically thinned specimens, which were twin jet electropolished to get the electron transparent region.

The working principles and apparatus details of the twin jet electropolishing system are given below, and the schematic details of the technique are shown in Fig. 2.17.

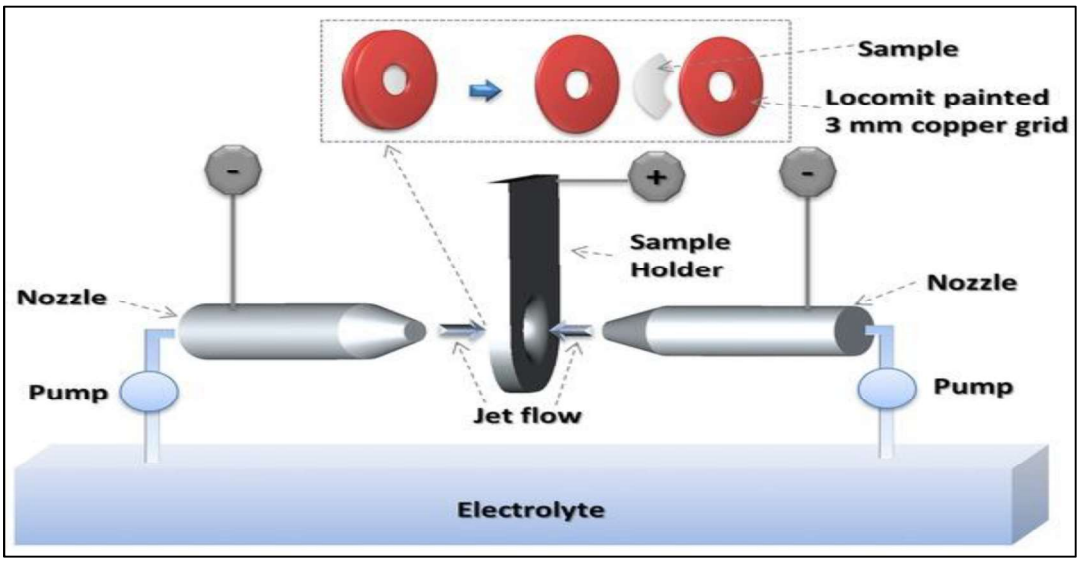

Fig. 2.17 Twin jet electro-polishing setup, and their working principle.

2.16.1 TEM sample preparation

Principle: to make a thin damage-free slice by thinning down a disc of a 3mm Dia, and 50-200 μm thick, until a central hole is obtained. At the microscope scale, the thin edge of the resulting dimple has parallel faces

Apparatus: The apparatus is made of an electrolytic cell immersed in a temperature-regulated chemical bath connected to a power supply for voltage and dissolution current regulation. The specimen holder ensures electrical contact and leaves both specimens' faces free. It is placed in a cell with the electrolytic jets targeted to each face center. Each jet nozzle is fitted with an electrode set at anode dissolution voltage. Perforation is detected by a photocell receiving a light beam emitted from the other side of the object.

Method: It is an electrochemical dissolution technique. The jet produces an increased action to the center of the specimen up to perforation. The result is a thin-edged perforation.

Action: It is based on electropolishing the conducting material. Electrochemistry is associated with the hydrodynamic action of an electrolyte jet. The viscous layer formed at

the specimen surface causes a differential etching of the relief and suppresses roughness. Material dissolution leaves a smooth and shiny surface.

Materials: The technique only applies to conducting materials such as metals and semiconductors. Materials must be bulk type, compact, and single-phased either fragile or ductile. It also applies to multi-phased and those containing the precipitates or the segregations. In these latter cases, the appropriate thinning condition can remain hard to define.

2.16.2 Transmission electron microscope

Transmission electron microscopy (TEM) represents a sophisticated method for characterizing nanostructured materials and thin films by capturing greatly magnified images through a parallel electron beam. This high-energy electron beam is accelerated using a voltage of around 200 kV. However, the electron energy can be tailored by adjusting the TEM to different voltages within the range of 80-300 kV. The operational principles of TEM closely resemble those of visible light microscopy, with the distinction that electrons are harnessed instead of light. While conventional light microscopy relies on the wavelength of visible light, which inherently limits image resolution to approximately 200 nm, TEM stands out due to its ability to manipulate electrons into much shorter wavelengths, thus delivering exceptional resolution.

In an optical microscope, the resolution is given by the Rayleigh criteria:

$$\theta = sin^{-1}(1.66 * \lambda\, d) \quad \text{.....Eq. 2.11}$$

Where 'λ' is the wavelength of the radiation, and 'd' is the aperture diameter. In contrast, TEM resolution relates to the wavelength of the electron beam. The electron wavelength is derived from the de Broglie relationship:

$\lambda = (h/ m*v)$……*Eq. 2.12*

Here, ‘h’ denotes Planck's constant, 'v' is the velocity of the electrons, and 'm' depicts the mass of the electrons. For instance, an electron beam accelerated at 200 kV yields an electron wavelength of roughly 0.0025 nm, as determined by the de-Broglie relationship. This minuscule wavelength contributes to TEM's exceptional spatial resolution. The foundational principles of TEM imaging involve a quantum mechanical interpretation of the interaction between the electron beam and the atomic potentials of materials. As the electron beam traverses the specimen, it undergoes diffraction or scattering along with a phase shift. The resultant transmitted or exit wave subsequently serves as the input for an underlying projection lens. This lens amplifies the exit wave's signal and projects it onto a fluorescent screen, creating an image. Fig. 2.18 shows an overall arrangement of the TEM and gives the schematic representation of its internal components.

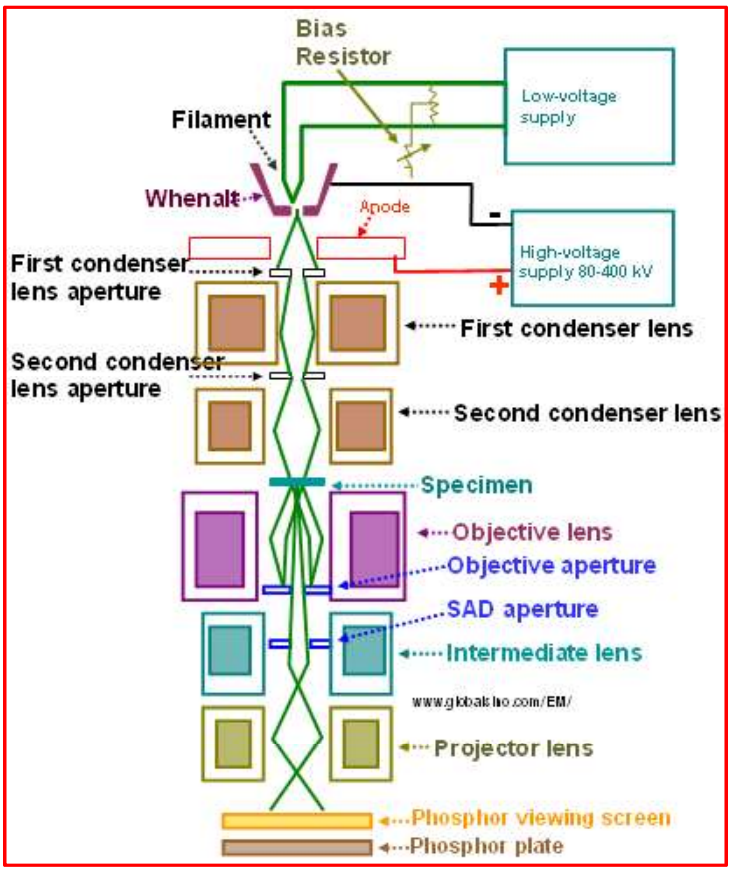

Fig. 2.18 Path of the electron beam in TEM, when high voltage is applied to electron source [190].

2.16.3 TEM Investigation of the metastable precipitates

The most potent approach for investigating the atomic arrangements at the bulk matrix, precipitates, and precipitate-matrix interfaces is High-Resolution Transmission Electron Microscopy (HRTEM). However, sample preparation of such a complicated methodology is a major challenge in HRTEM imaging. Before HRTEM analysis, the crystalline metallic material is delicately thinned down to a thickness of a few nanometres (around 50 microns) to make it transparent to the high-energy electron beam. This electron beam, operating at an acceleration of approximately 300/200 kV, is meticulously focused onto the specimen under scrutiny. These electrons are subsequently transmitted and diffracted based on the crystallographic characteristics of the material. The direct and diffracted electron beams

might interact either destructively or constructively, a phenomenon whose careful evaluation can unveil significant structural and chemical insights into bulk metallics/nanomaterials. This systematic pattern of constructive and destructive interactions is projected onto the imaging plane, manifesting as lattice fringes. Within these lattice fringes, phase contrast arises due to the interplay between constructive and destructive interactions. Constructive interference results from amplitude addition, while destructive interference emerges from amplitude subtraction. This intricate dance of amplitudes stems from the phase shift occurring between the transmitted and diffracted waves post their interaction. The outcome of this phenomenon is the acquisition of two-dimensional lattice fringe images, instrumental in extracting crystallographic and atomic-level details of diverse materials. Although the HRTEM technique, operating as a phase contrast microscopy, was initially introduced by Zernike at the University of Groningen, notably in the realm of optical microscopy, the same principle has found application in high-resolution TEM imaging. Over several decades, electron microscopy has gained prominence, yet its point-to-point resolution has evolved to approximately 0.16 nm. This remarkable progress has empowered the materials science community to elucidate materials' atomic structures. The integration of computational advances in materials science has further simplified accurate structure simulation. Moreover, simulating HRTEM images facilitates the localization of atom positions, achieved by comparing simulated images with experimental ones under optimal defocus and thickness parameters. X-ray Energy Dispersive Spectroscopy (XEDS) is instrumental in unravelling interface chemistry. However, instances of atomic column deformations inducing noise in HRTEM images necessitate image simulations for interpretation. Fortunately, smaller shifts (~0.01 nm) within the atomic lattice can be discerned in HRTEM images without difficulty.

Presently, the investigation of hetero-phase interphases in interconnects, semiconductors, optoelectronic devices, catalysts, solar cells, etc., through HRTEM poses a formidable challenge. Engineering materials often exhibit intricate hetero-phase interfaces. For instance, variations in lattice constants on either side of a hetero-phase interface might introduce an extra half-plane at the interface. The complexity deepens when the interaction of this extra half-plane across the interface results in misfit dislocation, whose Burgers vector differs from that of the bulk lattice dislocation due to the interface geometry. Before comprehending hetero-phase interfaces, a thorough analysis and understanding of well-defined interfaces in model structures are imperative. This foundation aids in grasping the intricacies of hetero-phase interfaces.

2.16.4 Diffraction contrast imaging

The concept of imaging based on diffraction contrast in crystalline/bulk metallic materials arises from the elastic coherent scattering of electrons which satisfies Bragg's angle. However, there exist two operational modes in TEM. The first one relates to the imaging mode. On the other hand, the second one is attributed to the diffraction mode. Diffraction contrast imaging stems from the interaction between both imaging and diffraction modes. To achieve a high-quality diffraction image, a condition known as the two-beam condition is favored in diffraction mode. By utilizing the Selected Area Diffraction (SAD) aperture to isolate a single diffracted beam during diffraction mode, a diffraction contrast image is generated within the imaging mode. The schematic representation of dual modes of operation, for instance, diffraction and imaging are shown schematically in Figs. 2.19a-b

Diffraction contrast imaging (DCI) is particularly valuable for examining defects in the material's interfaces and surfaces. Furthermore, this technique enables the acquisition of two distinct image types: a) bright-field images, and b) dark-field images. Bright-field images

are obtained by isolating the direct beam using the SAD aperture, whereas a dark-field image is generated by selecting any of the diffracted beams through the SAD aperture. Occasionally, the intensity of diffraction spots may exhibit variation due to local compositional differences in the material. Consequently, choosing such spots facilitates the identification of regions based on differences in contrast. The contrast in mass-thickness primarily relies on the atomic number (Z) or thickness of the investigated area. Regions with a higher atomic number or greater thickness appear dark in bright-field images and the reverse (bright contrast) is true for the dark-field images.

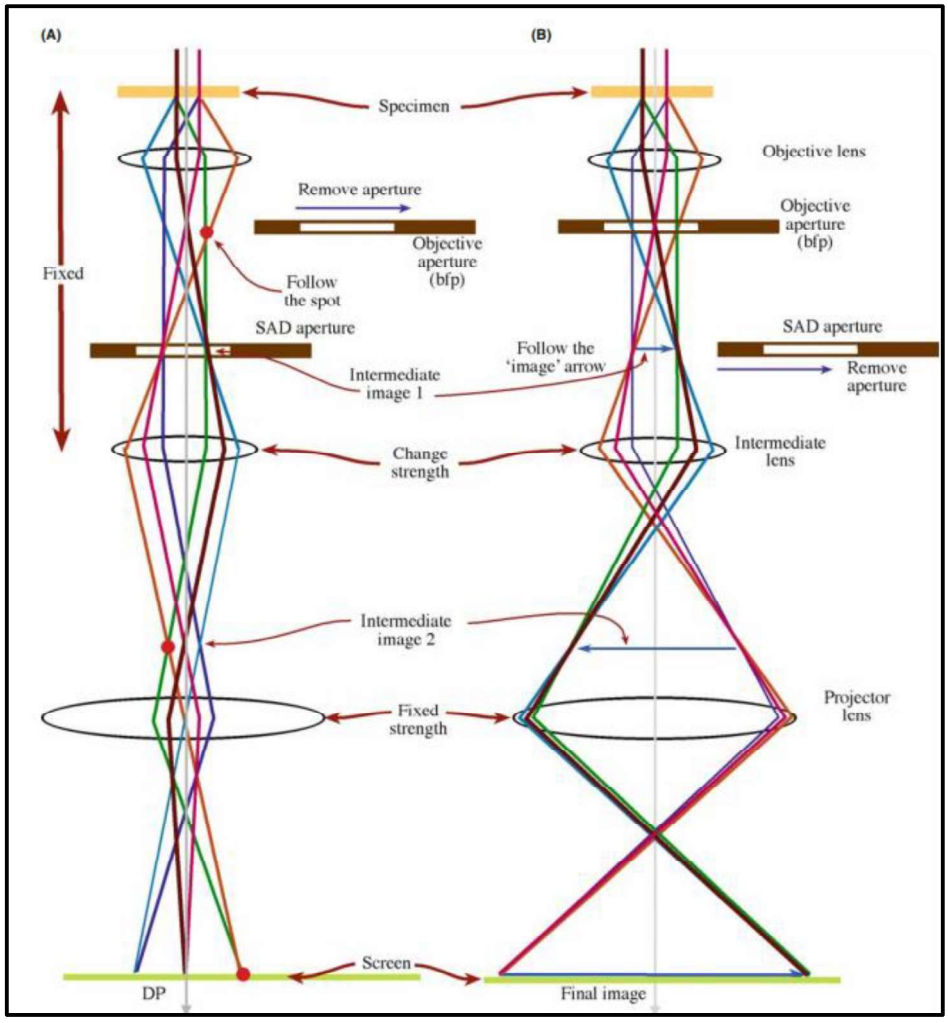

Figs. 2.19a-b Schematic of the imaging and diffraction mode of operation in TEM: (a) diffraction mode, and (b) imaging mode [190A].

2.16.5 Bright and dark-field TEM imaging

One of the primary distinctions between the bright-field and dark-field modes in Transmission Electron Microscopy (TEM) lies in the electron populations employed to construct the resulting images. The bright-field image is the more commonly generated image in TEM. In this mode, certain sections of the sample interact with electrons by either absorbing or scattering them, resulting in darker appearances, while areas allowing electrons to pass through display brighter features. The bright-field image is generated by selectively choosing the un-scattered (transmitted) electron beam via an aperture, thereby blocking the scattered electrons. This selection of the un-scattered beam leads to the depiction of regions containing crystalline structures or materials of higher mass as darkened regions. Conversely, in the dark-field mode, the aperture blocks the un-scattered electron beam, and instead, the scattered electrons are chosen. Consequently, regions, where electron scattering is minimal (such as the surroundings of the sample), appear as black regions, while materials present in the sample display brighter characteristics. This technique proves beneficial for improving contrast when the bright-field image lacks clarity, especially in scenarios where small crystalline features are challenging to discern or are obscured from view. Furthermore, the dark-field mode is valuable for investigating aspects like crystal lattice, defects within crystals, stacking faults, and dislocations, as well as particle and grain sizes, morphologies, and distribution of the precipitates. The schematic details of the bright and the dark field TEM imaging are given in Fig. 2.20a-b

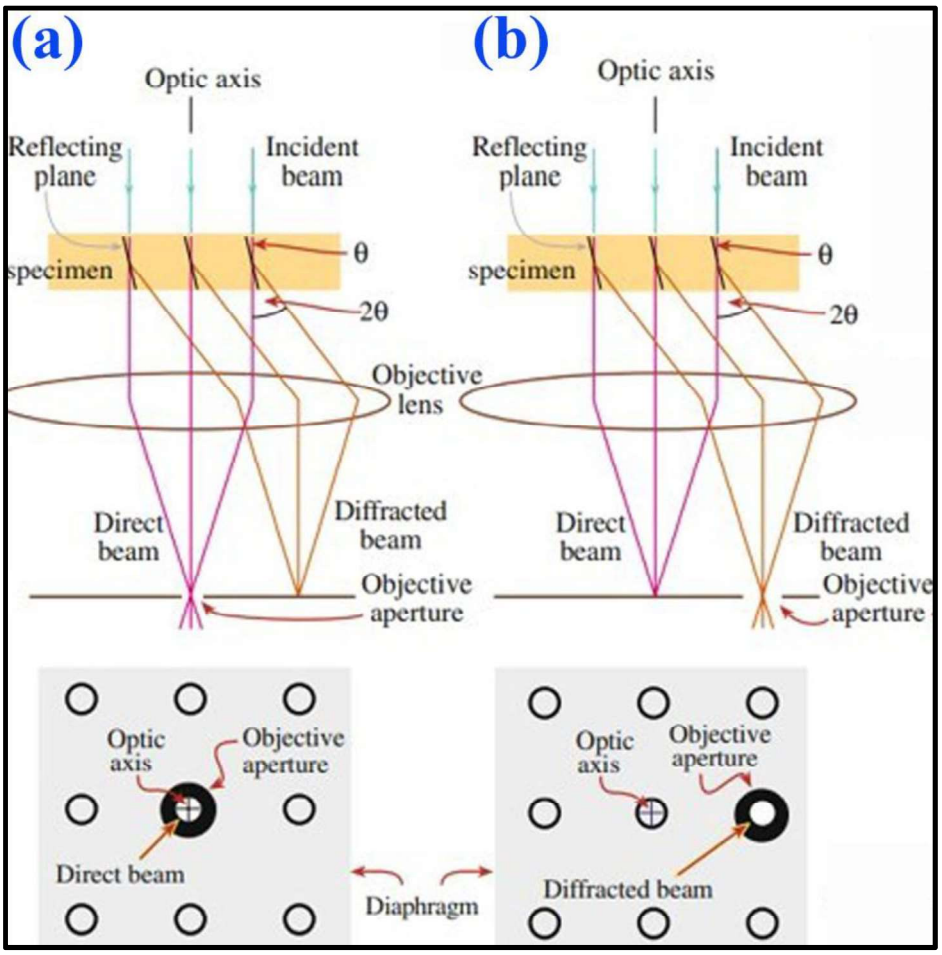

Figs. 2.20 a-b. Schematic of imaging technique: (a) bright-field TEM Imaging, (b) Dark field TEM Imaging [190B].

2.17 Weak-beam dark-field (WBDF) TEM imaging

Weak-beam dark-field transmission electron microscopy (WBDF-TEM) is an advanced imaging technique used to study the crystal defects and lattice strain in materials at the atomic scale. This technique is beneficial for analyzing imperfections in crystalline materials, such as dislocations, stacking faults, and other types of lattice distortions, and their working principles are given below:

2.17.1 Working principles

In conventional bright-field TEM imaging, a direct beam is used to illuminate the entire sample, and the transmitted electrons are collected to form an image. In weak-beam dark-field imaging, a weak electron beam is tilted to a specific angle relative to the crystal lattice planes of the sample. The tilting gives diffraction conditions that allow only a specific subset of diffracted beams to pass through the sample and reach the detector. The selected diffraction beam corresponds to reflections from crystal defects. The specific arrangement of weak-beam conditions creates contrast in the resulting image. Crystal defects, such as dislocations or stacking faults, cause a slight displacement of lattice planes compared to the perfect crystal lattice. When the tilted beam interacts with these defects, it creates diffraction patterns that are different from the patterns generated by the perfect lattice. These differences in diffraction patterns lead to localized dark spots in the image, highlighting the presence of defects. The technique involves tilting the specimens so that the lattice planes in most of the specimens are rotated away from Bragg's diffraction. This is done to create a condition, where only a small region around the defects satisfies Bragg's condition. Near the core of a dislocation or defect the lattice planes are locally bent back into Bragg condition. Fig. 2.21 shows WB conditions obtained after suitable tilting of the specimen (using the α and β). The weak spot g is a weak beam. On the other hand, sharp spots display a strong beam.

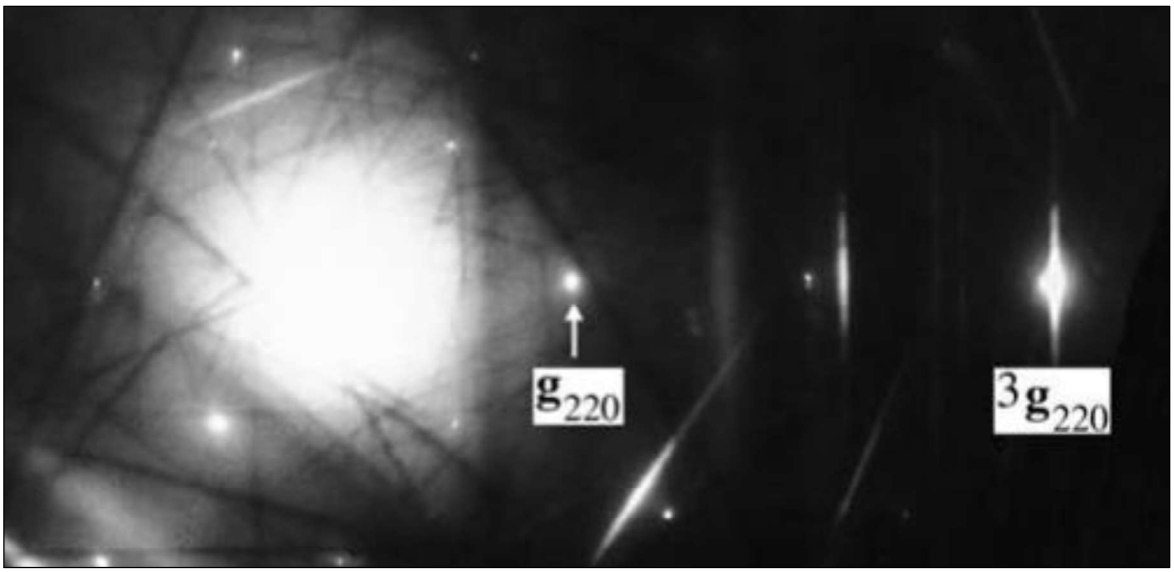

Fig. 2.21 Schematic of DPs in WB condition after suitable tilting, g (220) reflection is a weak beam, and 3g(220) shows the strong beam [190C].

As previously mentioned, WBDF TEM imaging is well-suited for visualizing defects or dislocations within the materials. The investigation of dislocations in the alloy structures plays a critical role in establishing the correlations between structure and properties, particularly in relation to the strain field. To conduct this study, six rectangular bar-shaped specimens were obtained from the as-received (AA7075T7352) alloy sheet, each with dimensions of 105 mm in length, 10 mm in width, and 7 mm in thickness. Additionally, six tensile specimens were extracted in accordance with the American Society for Testing of Materials-E8 (ASTM-E8) specifications, featuring a gauge length of 30mm, a width of 6 mm, and a thickness of 6 mm. The first three sets of the tensile samples were labelled as D1, while the remaining samples were designated as D2, D3, and D4. These tensile samples were cut from a heat-treated AA7075T7352 alloy sheet, with their length aligned parallel to the rolling direction of the sheet and their width parallel to the transverse direction. D1 underwent tensile straining until fracture to obtain maximum percentage elongation *(EL)* and a few other mechanical properties, such as yield strength (YS), and ultimate tensile strength

(UTS). Tensile data from the fractured specimens were plotted, and the UTS/YS ratio, along with the hardening exponent (n), was calculated using a curve-fitting approach. The mechanical properties were determined, including the standard deviation. The remaining three tensile specimens, D2, D3, and D4, underwent partial tensile straining to achieve true strains of 0.02, 0.06, and 0.1, respectively, all below the maximum percentage elongation. This was accomplished at a cross-head speed of 1mm/ minute using an Instron 5982 universal testing machine with a 100 kN capacity at room temperature. TEM samples were prepared from the gauge section of each partially strained specimen (D2, D3, and D4) under the same conditions as previously described for the TEM sample preparation. The thicknesses of the unstrained and tensile-strained specimens were kept consistent for TEM micrographic examination. The dislocation characterization was done using the TEM samples from the partially tensile-strained specimens with the help of weak-beam dark-field (WBDF) TEM imaging, following the methods illustrated above.

2.17.2 How to make WBDF TEM Imaging

The Kikuchi pattern is created by selecting the slightly thick region of the specimen and clicking on the diffraction to the touchpad. The specimen can be rotated using the Joystick to obtain the clear Kikuchi pattern. After suitable sample tilting, one may notice the intersecting bright and dark Kikuchi bands due to elastic and inelastic scattering of the electron. Following the particular Kikuchi band by suitable tilting of the α and β in touchpad, a series of linear and periodically arranged diffraction spots are obtained. In the particular value of α and β, two to three sharp and weak-ordered linear arrays of spots are obtained, and this is known as a weak beam condition. The sharp spots display the strong beam. On the other hand, weak spots show weak beams as represented in Fig. 2.22a-d. After getting the weak beam condition. Insert the objective aperture to bring “2g” or “3g” higher order of

weak spots on the optic axis making sure that no other spots are excited. One may also use the binocular to bring the particular diffracted spot in the optic axis. By removing the SAD aperture, and inserting the objective aperture the images obtained are the WBDF TEM micrograph.

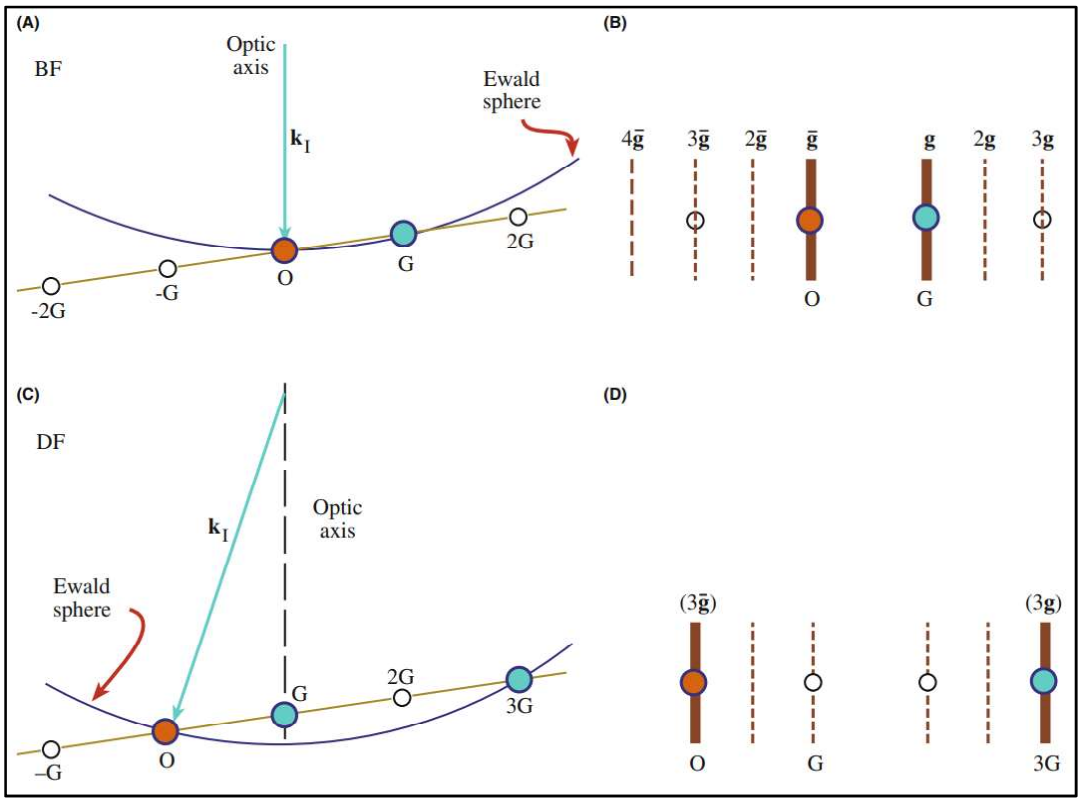

Figs. 2.22 a-d. The relationship between the orientation of the Ewald sphere, and the position of the Kikuchi lines: 0(g) (A and B) and g(3g) (C and D) in WB condition [190D].

2.18 Phase contrast imaging

HRTEM, an abbreviation for High-Resolution Transmission Electron Microscopy, is a method employed for conducting phase contrast imaging. The phase contrast image emerges from the interaction between the electron beams - one directly transmitted electron beam, and another diffracted electron beam as shown in the Fig. 2.23. In the HRTEM mode, both the direct and diffracted electron beams engage by either eliminating the objective aperture

or by utilizing the largest possible aperture size. These electron beams interact in a manner that alternates between constructive and destructive interference. This interaction results in the emergence of patterns, known as fringes, within the phase contrast image. The images produced through HRTEM are referred to as phase contrast due to the substantial phase shift experienced by the electron waves passing through a delicate specimen. Instances of phase contrast images include Moiré patterns, 1D or 2D lattice fringes, and Fresnel contrast at imperfections. The elucidation of these phase contrast images is not straightforward, as their contrast is influenced by various factors such as how the sample was prepared, the thickness of the specimen, the scattering characteristics, orientation, the degree of focus applied by the objective lens, as well as any present aberrations and astigmatism. Given that multiple beams contribute to the formation of phase contrast images, the spacing between lattice fringes becomes instrumental in deducing the atomic structure of the crystal. However, it's important to note that lattice fringes do not precisely represent atomic positions, although they can aid in identifying the phase. This is because the phase component is absent in the experimental phase contrast image. Consequently, accurately comprehending phase contrast images, along with information like atomic positions, atomic structure at interfaces, and defects, necessitates the utilization of multi-slice simulations and computational methodologies.

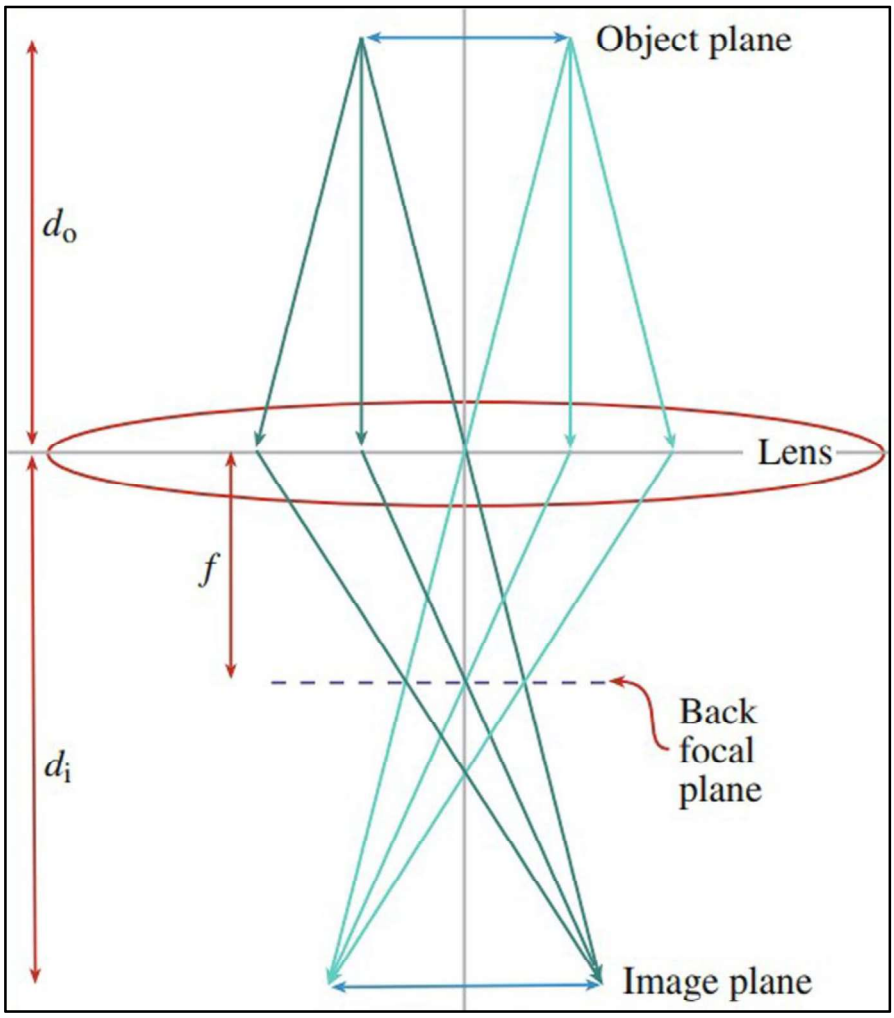

Fig. 2.23. Schematic of HRTEM mode of operation (phase contrast imaging) [190E].

2.19 HAADF STEM or Z-contrast imaging

Contrast can be quantitatively defined by measuring the difference in intensity (Δ) between adjacent areas. Z-contrast is a high-resolution imaging technique based on atomic mass-thickness (Z) imaging. In this technique, detectable scattering arises from individual atoms or columns of atoms. The Annular Dark Field (ADF) detector generates images by collecting low-angle elastically scattered electrons. HAADF STEM (High-Angle Annular Dark Field Scanning Transmission Electron Microscopy) is an imaging technique in which the specimen is scanned with an electron probe. In HAADF STEM, images are formed by

directly mapping the intensity of electrons scattered at high angles. The electrons scatter at high angles, making them incoherent with respect to the source electrons. Consequently, HAADF STEM or Z-Contrast images are inherently incoherent. The primary advantage of this imaging technique is its exceptionally high resolution. Z-contrast or HAADF STEM images are considered direct representations of the scattering power at the atomic level. The scattering power is determined by the square of the atomic number (Z) and the scattering cross-section. The incoherent nature of these images eliminates the possibility of phase differences during imaging, providing real-space information. This eliminates the need for extensive simulations and computational trials to fit structural models. The details of HAADF-STEM or Z-contrast imaging are illustrated in Fig. 2.24.

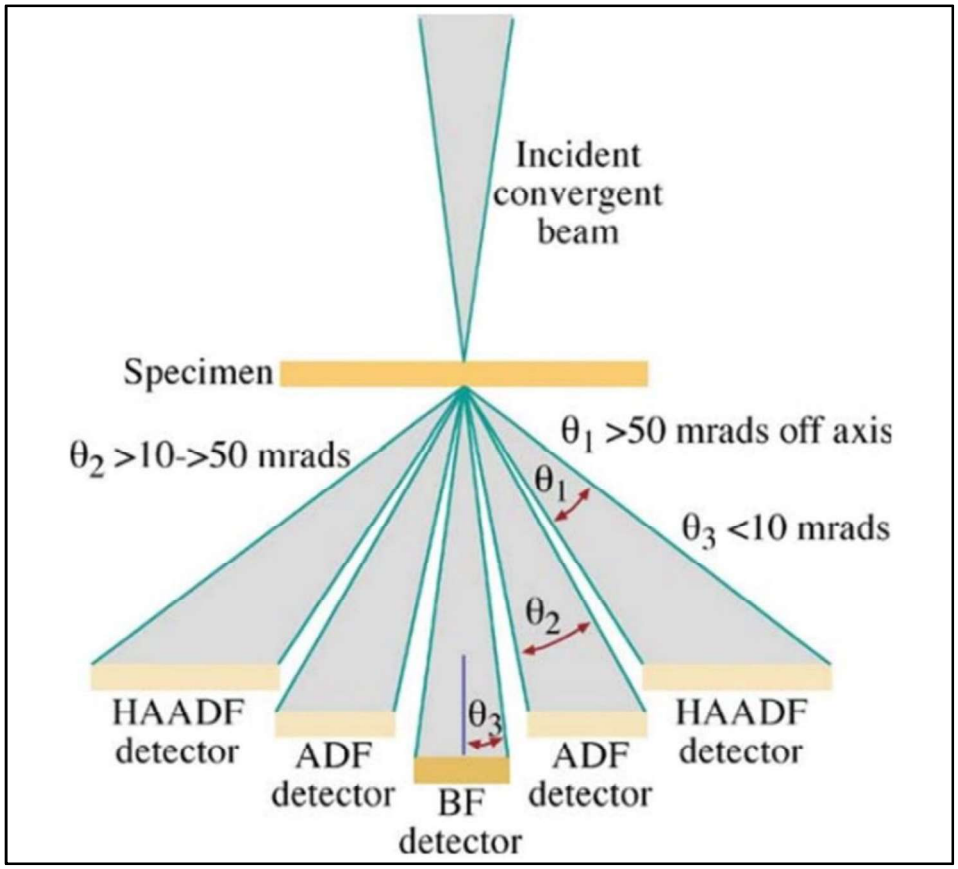

Fig. 2.24 Schematic representation of HAADF-STEM or the Z-contrast imaging [190F].

2.20 X-ray energy dispersive spectroscopy (XEDS)

The method involves the utilization of X-rays that are emitted from the specimen when the electron beam displaces the inner-shell electrons of the atoms within the sample. This displacement triggers an energy transition as the vacant states left by the displaced electrons are filled through higher-energy electrons. This energy transition results in the emission of X-rays, with each emitted X-ray having a specific energy level represented as spectral peaks. Each of these peaks provides elemental information based on the unique characteristics of X-ray energy. The collective chemical information is gathered and presented in the form of an EDS (Energy-Dispersive X-ray Spectroscopy) spectrum. Moreover, X-ray EDS (XEDS) is highly effective for mapping the distribution of chemical species within the material. This information is visually conveyed through STEM-EDS elemental mapping. XEDS forms the foundational component of analytical microscopy, aiding in the determination of chemical composition and the mapping of elements within materials at the atomic level. To facilitate the process, a schematic of the EDS detector used for elemental mapping in STEM mode, alongside several other detectors, is given in Fig. 2.25.

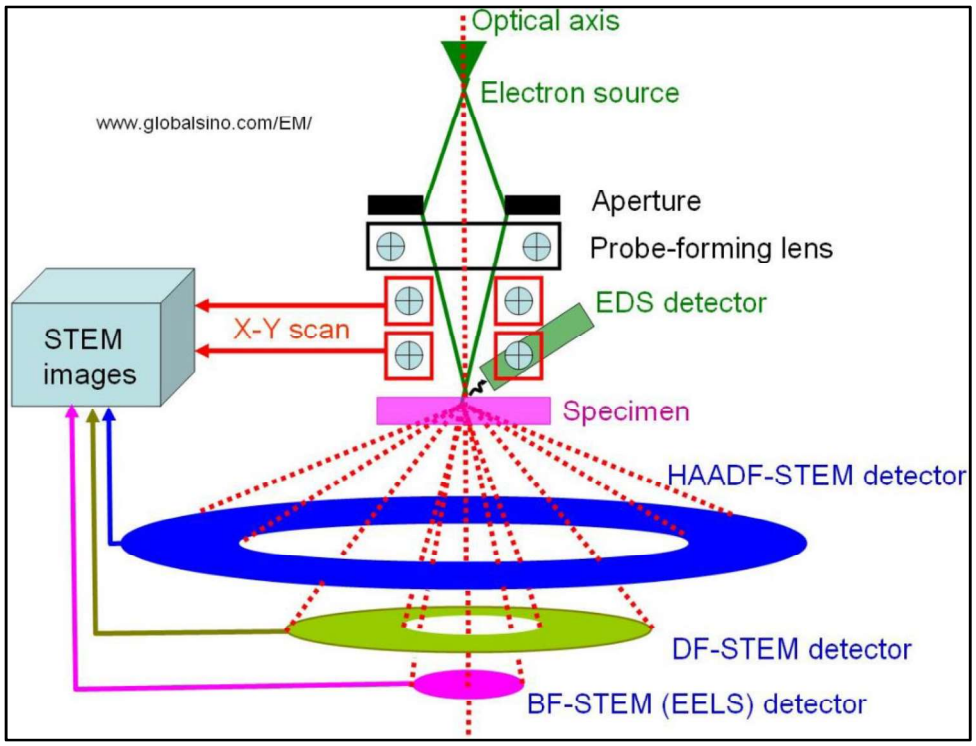

Fig. 2.25 Schematic of STEM EDS detector, and a few other detectors used for the analytical characterization [190].

2.21 Mechanical characterization

2.21.1 Conventional hardness test

In practice, hardness is measured in terms of the size of the impression made on a specimen by an indenter of a specified shape when a specific load is applied for a specific dwell time. The indent being is measured after the force has been removed. There are four standard methods for expressing the relationship between the hardness and the indentation size These are Brinell Hardness (BHN), Knoop Hardness (KH), Rockwell Hardness, and Vickers Hardness (VHN). In the current study, we extensively used the Vickers Microhardness Test to measure the hardness of the materials

2.21.2 Vickers microhardness

In this test, a diamond indenter in the form of a square-based pyramid with an angle of 136º between the opposite faces at the vertex is pressed into the surface of the test piece using force, F (Newton, range ~1kg to 120kg) applied for a dwell time of 15 seconds. Once the force has been removed, the diagonal length of the residual imprint d_1 (mm) and d_2 (mm) are measured. The Vicker's hardness (Hv) is proportional to the test force divided by the surface area of the indentation, which can be calculated using *Eq. 2.13* [190 G].

$$H_V = 0.102*[(2F\,Sin(\alpha/2))]/d^2 \quad \ldots\ldots\ldots\ldots\ldots\ldots\ldots\ldots\ldots\ldots\ldots\ldots\ldots\ldots Eq.\ 2.13$$

Here, d is the arithmetic mean in mm of the two diagonal lengths, d_1 and d_2. The α is the angle between the opposite faces at the vertex of the pyramidal indenter (136º), and F is the test force in Newton. This hardness test is mainly used for the metals. Moreover, if a low load is applied, it can also be used for the hardness measurement of the ceramics.

2.21.3 Instrumented microhardness test

The difference between the Vickers microhardness and instrumented microhardness is attributed to the contact area between the indenter and the specimen being tested. The Vickers microhardness is obtained from the developed area, which is practically measured under the microscope. On the other hand, Instrumented hardness (H_{IT}) can be calculated from the projected area (Ap) as reported in the literature [190 G].

$$H_{IT} = F/A_p \quad \ldots\ldots\ldots\ldots\ldots\ldots\ldots\ldots\ldots\ldots\ldots\ldots\ldots\ldots\ldots\ldots\ldots\ldots Eq.2.14$$

The Vickers hardness (H_V) is calculated from the developed area A_d.

$$H_V = 0.102*[F/A_d] \quad \ldots\ldots\ldots\ldots\ldots\ldots\ldots\ldots\ldots\ldots\ldots\ldots\ldots\ldots\ldots\ldots\ldots\ldots Eq.2.15$$

The relationship between the A_d and A_p is given below:

$A_d = A_p Sin\alpha$……*Eq.2.16*

Here, α is the angle between the axis of the indenter and one of the faces of the projected area of the pyramid.

2. 21.4 Tensile test and work hardening behavior

A tensile test is a mechanical test used to determine the mechanical properties of a material, particularly its tensile strength, yield strength, elongation, and modulus of elasticity. During a tensile test, a specimen of the material is subjected to an axial pulling force (tensile force) to measure how it responds to the applied load. This test helps to assess a material's ability to withstand stretching or elongation without breaking, which is crucial information for materials engineering and design applications.

The results of the tensile test provide valuable insights into a material's behavior under tension and are used in various industries, including manufacturing, construction, and materials research. For this test, the 110 x 12 x 5 mm^3 dimensions of the specimens are extracted from the heat treated (T4, T6, T73, and T7352), cold deformed to three different amounts (15%, 30% and 45%), and subjected to the peak-ageing (ageing at 120ºC for 24hrs). The tensile specimens of the ASTM E8 standard (Fig. 2.27) are made using the electric discharge machining system. The tensile test is performed in the Instron universal testing machine (Instron 5982, 100kN) till failure at the strain rate of 10^{-3}/ sec. Engineering stress-engineering strain data is plotted, and tensile properties *(%EL, YS, and UTS*) are determined by taking the average value of the fractured specimens. The *UTS/YS* ratio, work hardening exponent *(n),* and strength-coefficient *(K)* are determined. The flow behavior of the alloy

was studied using various mathematical models proposed by Hollomon, Ludwik, Ludwigson, Swift, and Voce. One of the best-fitted flow curve parameters was determined for the structure-property correlations.

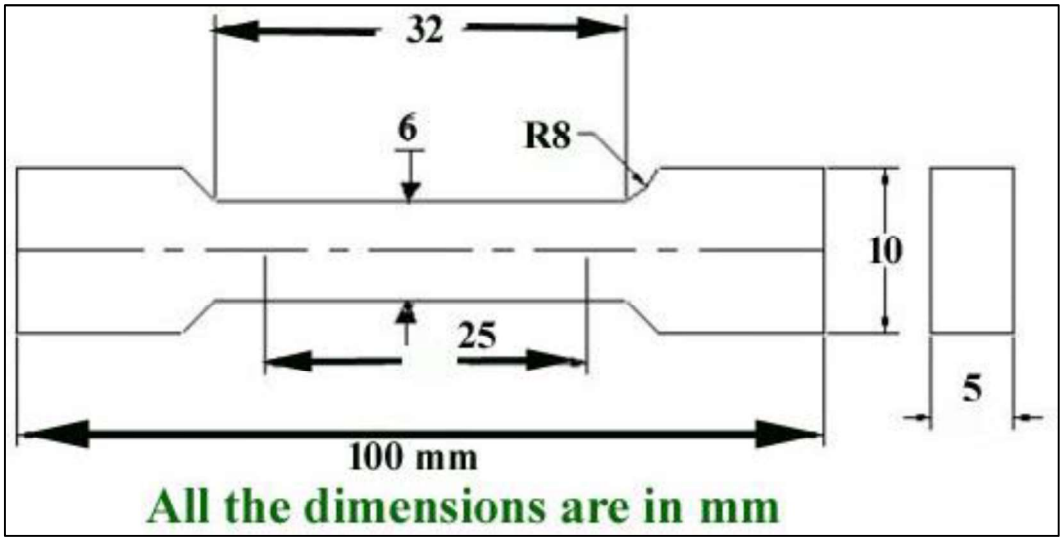

Fig. 2.26 Schematic details of tensile specimens (all dimensions are in mm)

2.21.5 Stress corrosion cracking (SCC)

Stress corrosion cracking (SCC) is a specific type of corrosion-related failures that occur in certain materials when they are subjected to combinations of tensile stress and a corrosive environment. Unlike some other forms of corrosion, SCC can result in sudden and catastrophic failures making it a significant concern for various industries, including aerospace, nuclear, and chemical process.

For this, a total of sixteen pieces (four of each heat treatment: T4, T6, T73, and T7352) of tensile specimens (80mm x10mm x 3mm) were made as per the ASTM E-8 standard (Fig. 2.27). To determine the stress corrosion cracking (SCC) behavior of AA7075T7352 in an as-received state, as well as in another heat-treated condition (T6, and T73), the samples were tested using the slow strain rate tensile test, in the air and 3.5% NaCl solution.

The tests were performed using a *100 kN (Instron 5982)* universal testing machine at a prolonged strain rate of $1x10^{-6}$/ second. The relative plasticity loss can be defined as a stress corrosion cracking susceptibility, which can be estimated as [190 H]:

$I_{SSRT} = 1-[(\delta_S)/ (\delta_A)]$ ……*Eq. 2.17*

Here, I_{SSRT} = stress corrosion sensitive co-efficient, the δ_S, and δ_A are total elongation in 3.5% NaCl solution, and in the air.

Software details:

MatLab: The software was used for the bulk texture analysis: pole figure (PF), orientation distribution function (ODF), and determination.

Image J: Used for the precipitates, and the grain size calculation diffraction pattern analyses.

Vesta: Structural characterization of the materials

Origin 18: Phase analysis, XRD pattern analyses

JEMS: structural analysis of materials, diffraction pattern simulation, crystallography, crystal system determination, HR TEM analyses.

Expert high score, and Expert texture: phase analysis, residual stress, ODF, Pole Figure

Thermo Calc: Phase diagram analyses, liquidus to solidus temperature determination